nature cancer

Article

https://doi.org/10.1038/s43018-024-00768-3

Identification of a clinically efficacious CAR T cell subset in diffuse large B cell lymphoma by dynamic multidimensional single-cell profiling

Received: 4 May 2023

Accepted: 10 April 2024

Published online: 15 May 2024

Check for updates

Ali Rezvan[1], Gabrielle Romain[1], Mohsen Fathi[2], Darren Heeke[3], Melisa Martinez-Paniagua[1], Xingyue An[1], Irfan N. Bandey[1], Melisa J. Montalvo[1], Jay R. T. Adolacion[1], Arash Saeedi[1], Fatemeh Sadeghi[1], Kristen Fousek[4], Nahum Puebla-Osorio[5], Laurence J. N. Cooper[2], Chantale Bernatchez[6], Harjeet Singh[7], Nabil Ahmed[4], Mike Mattie[3], Adrian Bot[3], Sattva Neelapu[5] & Navin Varadarajan[1]

Chimeric antigen receptor (CAR) T cells used for the treatment of B cell malignancies can identify T cell subsets with superior clinical activity. Here, using infusion products of individuals with large B cell lymphoma, we integrated functional profiling using timelapse imaging microscopy in nanowell grids with subcellular profiling and single-cell RNA sequencing to identify a signature of multifunctional $CD8^+$ T cells (CD8-fit T cells). CD8-fit T cells are capable of migration and serial killing and harbor balanced mitochondrial and lysosomal volumes. Using independent datasets, we validate that CD8-fit T cells (1) are present premanufacture and are associated with clinical responses in individuals treated with axicabtagene ciloleucel, (2) longitudinally persist in individuals after treatment with CAR T cells and (3) are tumor migrating cytolytic cells capable of intratumoral expansion in solid tumors. Our results demonstrate the power of multimodal integration of single-cell functional assessments for the discovery and application of CD8-fit T cells as a T cell subset with optimal fitness in cell therapy.

The administration of immune effector cells propagated ex vivo has been shown to be effective for the treatment of solid tumors, such as melanomas, and liquid tumors, such as acute and chronic B cell leukemias[1,2]. T cells stably endowed with a genetically encoded chimeric antigen receptor (CAR) targeting CD19 have shown remarkable clinical responses in individuals with B cell lineage leukemias and lymphomas who were refractory to other treatments. This has spurred the development of CARs targeting antigens other than CD19 to treat hematologic malignancies and invasive cancers[3–5]. The field of CAR T cells has exploded with the culmination of the Food and Drug Administration (FDA) approval of CAR T cell products, and, while attention has been devoted to antigen discovery and CAR design[2,3,6], identifying metrics that define the functional potential and thus the therapeutic potential of T cell products is limited[7–9].

Because of inter- and intratumor heterogeneity, technologies that aggregate T cell biology are unable to accurately capture the

[1]Department of Chemical and Biomolecular Engineering, University of Houston, Houston, TX, USA. [2]CellChorus, Houston, TX, USA. [3]Kite, a Gilead Company, Santa Monica, CA, USA. [4]Texas Children's Hospital, Baylor College of Medicine, Houston, TX, USA. [5]Department of Lymphoma and Myeloma, The University of Texas MD Anderson Cancer Center, Houston, TX, USA. [6]Department of Biologics Development, The University of Texas MD Anderson Cancer Center, Houston, TX, USA. [7]Divsion of Pediatrics, The University of Texas MD Anderson Cancer Center, Houston, TX, USA. e-mail: nvaradar@central.uh.edu

https://doi.org/10.1038/s43018-024-00768-3

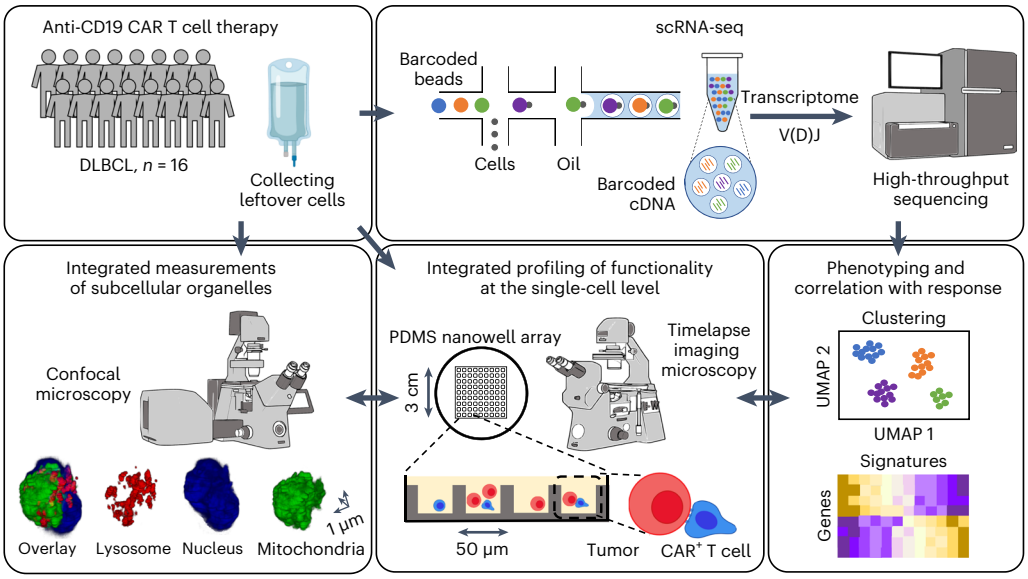

Fig. 1 | Study design for integrated single-cell multiomic profiling of IPs. Overview of the experimental design for profiling the residual CAR T cell IPs of 16 individuals with DLBCL (nine CR and seven PR/PD). Cells were used for scRNA-seq analysis, confocal microscopy and TIMING; PDMS, polydimethylsiloxane.

complexities of an infusion product (IP) with defined and desired characteristics. For example, populations of less differentiated cells (central memory or stem memory T cells) have increased proliferative capacity, leading to sustained presence, but individual cells vary in their persistence and functional potential[10–12]. Although persistence of infused T cells correlates with antileukemic effects, preclinical data suggest that the ability of cells to recycle effector function within the tumor microenvironment is an essential attribute for tumor eradication[13,14]. Single-cell RNA sequencing (scRNA-seq) has emerged as a powerful technique to identify T cell heterogeneity, but scRNA-seq is unfortunately a destructive method that cannot directly assay function and interaction with tumor cells. For example, CAR T cells that participate in killing and serial killing can be prone to activation-induced cell death, severely limiting their antitumor potential[15,16]. Integrating functional and molecular profiling can uncover the molecular characteristics of T cells with optimal antitumor functions and will directly impact the discovery, manufacture and translation of cell-based therapies.

We developed multiomic dynamic profiling to understand the heterogeneity of individual CD19-specific CAR T cells within axicabtagene ciloleucel (axi-cel) IP administered to individuals with diffuse large B cell lymphoma (DLBCL). By integrating function, phenotype, transcriptional profiling and metabolism, we have identified and validated a subset of $CD8^+$ T cells, termed CD8-fit T cells, that are correlated with clinical responses. Functionally, CD8-fit T cells are serial killer T cells endowed with migratory capacity and mitochondrial fitness, independent of CAR designs and manufacturing protocols.

Results

Responder IPs are enriched in migratory T cells

To investigate the importance of CAR T cell characteristics, we used cells from IPs of individuals with DLBCL who received anti-CD19 CAR T cell therapy. In total, samples from 16 individuals were collected and tested at the single-cell level using timelapse imaging microscopy in nanowell grids (TIMING), confocal microscopy and scRNA-seq (Fig. 1). At a follow-up of 6 months after treatment, nine individuals showed a complete response (CR), and seven showed either a partial response (PR) or progressive disease (PD).

T cells from the IP showed uniformly high viability (87–93%), and phenotypic characterization of the CAR T cells by flow cytometry showed no differences in frequency of CAR expression (40–80%) and a balanced $CD4^+$/$CD8^+$ T cell distribution (Extended Data Fig. 1). We used the TIMING platform to dissect functional heterogeneity at the single-cell level across these 16 IPs. At an effector-to-target (E:T) ratio of 1:1, the frequency of killing and the dynamics of the interaction between the T cell and the tumor cell leading to killing were largely conserved, consistent with the expectation that intrinsic T cell killing mechanisms are not different between the two groups of responders (Supplementary Table 1, Extended Data Fig. 2a–c and Supplementary Video 1). We next evaluated the ability of T cells to recycle effector (lysis) function by examining nanowells with an E:T ratio of 1:2 and observed that the frequency of serial killer T cells was significantly enriched in IPs associated with clinical response (Fig. 2a, Extended Data Fig. 2d and Supplementary Videos 2 and 3).

Adoptive T cell therapy relies on the cells to actively migrate to seek and destroy tumors. We accordingly measured the migratory potential of T cells using TIMING. In nanowells that lacked tumor cells (E:T of 1:0), the average T cell migration (persistent motility for at least one body length, hereafter 'migration') was significantly increased in IPs associated with CR (Fig. 2b). Aggregated by response, T cells from individuals with CR showed a significantly faster migration than T cells from individuals with PR or PD at the single-cell level (Fig. 2b and Supplementary Video 4). Similarly, even within 1:1 (E:T) nanowells, single T cells from individuals with CR showed enhanced migration, both with and without conjugation to tumor cells, compared to T cells from individuals with PR or PD (Fig. 2c and Supplementary Video 5). We next pooled T cells from all IPs (E:T of 1:1 nanowells, regardless of clinical response), and this comparison confirmed that migration is an intrinsic feature of killer T cells compared to nonkiller T cells and that these properties are independent of CD8 expression (Fig. 2d, Supplementary Video 6 and Extended Data Fig. 2f).

We integrated TIMING with three-dimensional (3D) confocal microscopy to interrogate the correlation between migration, killing and organelle volume within IP T cells. We constructed the image of each live cell as a series of stacks in 3D to capture the mitochondrial volume (a known feature of proliferative capacity)[17], lysosomal volume (including secretory lysosomes that contain perforin/granzymes) and the nucleus (cell size). When T cells from the IPs were stratified by clinical response, those from individuals with CR had increased mitochondrial and lysosomal volume compared to T cells from individuals with PR or PD (Fig. 2e). Because IP T cells from each individual

had been characterized by both TIMING and confocal microscopy, we investigated the correlation between migration and mitochondrial and lysosomal volumes. We observed a linear correlation between migration and mitochondrial volume (Pearson correlation = 0.62, $P = 0.01$) and between migration and lysosomal volume (Pearson correlation = 0.66, $P = 0.006$; Fig. 2f). We performed unsupervised hierarchical clustering of all the dynamic parameters from TIMING and the organelle measurements from confocal microscopy. Clustering showed that serial killing, migration and increased mitochondrial and lysosomal volume were features associated with T cells from individuals who achieved CR (Extended Data Fig. 2e). Collectively, these functional single-cell measurements illustrate that in comparison to IP T cells from individuals with PR or PD, IP T cells from individuals with CR are enriched in a subpopulation of T cells that balance migration, serial killing and mitochondrial fitness.

CD8-fit: a signature of functional T cells in responder IPs

To understand the molecular basis of these observations, we performed scRNA-seq of 21,469 $CD3^+$ T cells from nine individuals (four with CR and five with PD). We defined ten clusters of T cells (T1–T10) based on their molecular properties, and cells derived from individuals with both CR and PD were represented in all the clusters (Extended Data Fig. 3a).

Within the IP T cells, we did not observe significant expression of either well-established genes associated with T cell exhaustion, including *TOX*, *PDCD1* and *CD38*, or emerging regulators like *ID3* and *SOX4* within any of our T cell clusters (Extended Data Fig. 3b)[8,18]. We first focused the analysis on $CD8^+$ T cells. Specifically, we performed unsupervised clustering based on differentially expressed genes (DEGs) and identified seven clusters (Fig. 3a). Clusters CD8-1 and CD8-2 were comprised predominantly of cells from individuals with PD, whereas cluster CD8-6 was predominantly comprised of cells from individuals with CR (Fig. 3b). T cells within the CD8-6 cluster showed a high expression of genes associated with effector functionality, including cytotoxicity (*GZMB*, *GNLY*, *PRF1*, *FASLG* and *NKG7*), cytokines and chemokines (*CCL3-5* and *IFNG*) and migration (*MYH9*, *RHOH* and *RHOC*; Fig. 3b,c). Within the cytotoxic molecules, *GZMH* more so than *GZMB* or *GZMA* was significantly upregulated in cluster CD8-6 (Fig. 3c). Cells in the CD8-6 cluster were significantly enriched in pathways associated with T cell antigen receptor (TCR) activation, PGC1α/mitochondrial biogenesis, actin cytoskeleton regulation and migration (RHO pathway; all P values of $<2.2 \times 10^{-16}$; Fig. 3b). To map the relationships between these clusters, we performed pseudotime analysis of the three CD8 clusters. We observed two distinct fates stemming from the central memory-dominant cell cluster (CD8-2): a central memory/effector memory-dominant branch (CD8-1) and an effector memory-dominant branch (CD8-6; Extended Data Fig. 3c). Because the activation of AMP kinase (AMPK) through phosphorylation is known to regulate PGC1α/mitochondrial biogenesis, lysosomal biogenesis and migration through cytoskeleton reorganization[19–21], we explored if AMPK activation was one of the key molecules to integrate our functional observations. We performed single-cell gene set enrichment analysis (ssGSEA) and showed that phosphorylated AMPK activity (as measured through direct inhibition of carbohydrate response element binding protein activity) was significantly enriched in the CD8-6 cluster compared to in the CD8-1 and CD8-2 clusters ($P < 2.2 \times 10^{-16}$; Extended Data Fig. 3d).

To determine if the CD8-6 cluster includes the multifunctional migratory serial killer T cells observed in the IP by TIMING (Fig. 2a), we took advantage of the recently published molecular signature of both killer and persistent serial killer $CD8^+$ T cells (Supplementary Table 2)[22]. These signatures were derived by identifying serial killer, killer and nonkiller healthy donor-derived CD19-specific CAR T cells using TIMING and then performing single-cell gene expression profiling on the same cells retrieved using a Sartorius CellCelector micromanipulator robot[22]. We performed ssGSEA and showed that cells within the CD8-6 cluster harbor the signatures of functionally validated killer and multifunctional serial killer T cells that express *CD2* (Fig. 3d)[9,22]. Similarly, CD8-6 cells also showed enrichment in a *TCF7* gene signature (Supplementary Table 2) associated with enhanced in vivo persistence compared to $CD8^+$ T cells from individuals with PD (Extended Data Fig. 3d)[23]. Based on integrating the functional and molecular features at single-cell resolution, CD8-6 cells exhibited features of migration, serial killing and mitochondrial fitness and were relabeled as CD8-fit T cells. Collectively, scRNA-seq showed that $CD8^+$ T cells from individuals who achieved CR were enriched in CD8-fit T cells that were not exhausted and were endowed with migratory capacity, mitochondrial fitness and serial killing.

CD8-fit T cells are linked to tumor persistence and clinical responses

To validate the enrichment of CD8-fit T cells with clinical responses, we used two other publicly available axi-cel scRNA-seq IP datasets[8,24]. In both datasets, the CD8-fit T cell subpopulation was enriched in individuals who achieved CR (Fig. 3e). We next investigated whether CD8-fit T cells possess molecular signatures associated with persistence and proliferation in vivo after infusion, a key attribute of CAR T cells associated with efficacy. Using the TCR as a barcode, a recent study derived the molecular signature of IP CAR T cells that can proliferate in vivo (Extended Data Fig. 3e)[25]. Quantitative mapping of the similarity between the molecular profiles of cells of the IP CAR T cells from the reference dataset to our dataset (Supplementary Table 3) showed that cells of the CD8-fit T cell cluster harbor signatures of cells that longitudinally persist in individuals after treatment (Extended Data Fig. 3f,g).

To validate T cell migration, we curated a collection of 40 genes (labeled T cell migration score; Supplementary Table 2) with documented roles in actin cytoskeleton remodeling in T cells[26], including *RHOA* and *MYH9* (actomyosin contraction), *TLN1* and *VCN* (actin–integrin interplay) and *MYO1G* (actin contraction). $CD8^+$ T cells from individuals who achieved CR showed a significant enrichment in the T cell migration score compared to $CD8^+$ T cells from individuals who had PD (Fig. 3f). Cluster-wise analyses using ssGSEA confirmed that the T cell

Fig. 2 | T cells from individuals with CR were enriched for migration, serial killing and mitochondrial volume compared to T cells from individuals with PR/PD. a, Left, schematic of a serial killing event wherein a CAR T cell conjugates and kills two NALM-6 cells. Right, comparison of serial killing by T cells from either individuals with CR ($n = 9$ IPs) or individuals with PR or PD ($n = 7$ IPs) within all 1:2 (E:T) nanowells. Each dot (n) represents the frequency of serial killing for a single IP. Bottom, micrograph showing a serial killing event through the 6 h of timelapse imaging. The dotted line represents the median in the violin plot, and the P value was computed using a two-tailed Mann–Whitney test. **b**, Left, schematic of the migration for a CAR T cell. Middle, each dot (n) represents the average T cell migration for each IP (CR: $n = 9$ IPs; PR/PD: $n = 7$ IPs; E:T of 1:0). Right, comparison between all T cells by response. Bottom, micrograph showing a T cell with high (2 μm min^{-1}) and low (0.2 μm min^{-1}) migratory capacity. **c**, Left, schematic of a CAR T cell migrating with/without conjugation to a NALM-6 cell (E:T of 1:1). Right, comparison between the migration of CR and PR/PD CAR T cells within all 1:1 (E:T) nanowells. Bottom, micrograph showing a CAR T cell migrating before/during conjugation. **d**, Left, schematic of a CAR T cell migrating before conjugation with a NALM-6 cell (E:T of 1:1) in killer and nonkiller CAR T cells. Right, comparison between the migration of killer and nonkiller CAR T cells within all 1:1 (E:T) nanowells. Bottom, micrographs showing killer and nonkiller CAR T cells. **e**, Comparisons of the sizes of mitochondria and lysosomes between T cells derived from either CR or PR/PD IPs. The confocal 3D image on the right illustrates a representative example of the nucleus (blue), total mitochondria (green) and lysosomes (red). **f**, Correlation between average organelle size and average migration (E:T of 1:1, without conjugation) of T cells. Each dot represents the average value for T cells from a single IP (CR: $n = 9$ IPs; PR/PD: $n = 7$ IPs). P values and Pearson correlation coefficients were calculated for the linear regressions. Error bars represent s.e.m. For all violin plots, the black bars represent the median, the dotted lines denote quartiles, and P values were computed using two-tailed Welch's t-tests.

https://doi.org/10.1038/s43018-024-00768-3

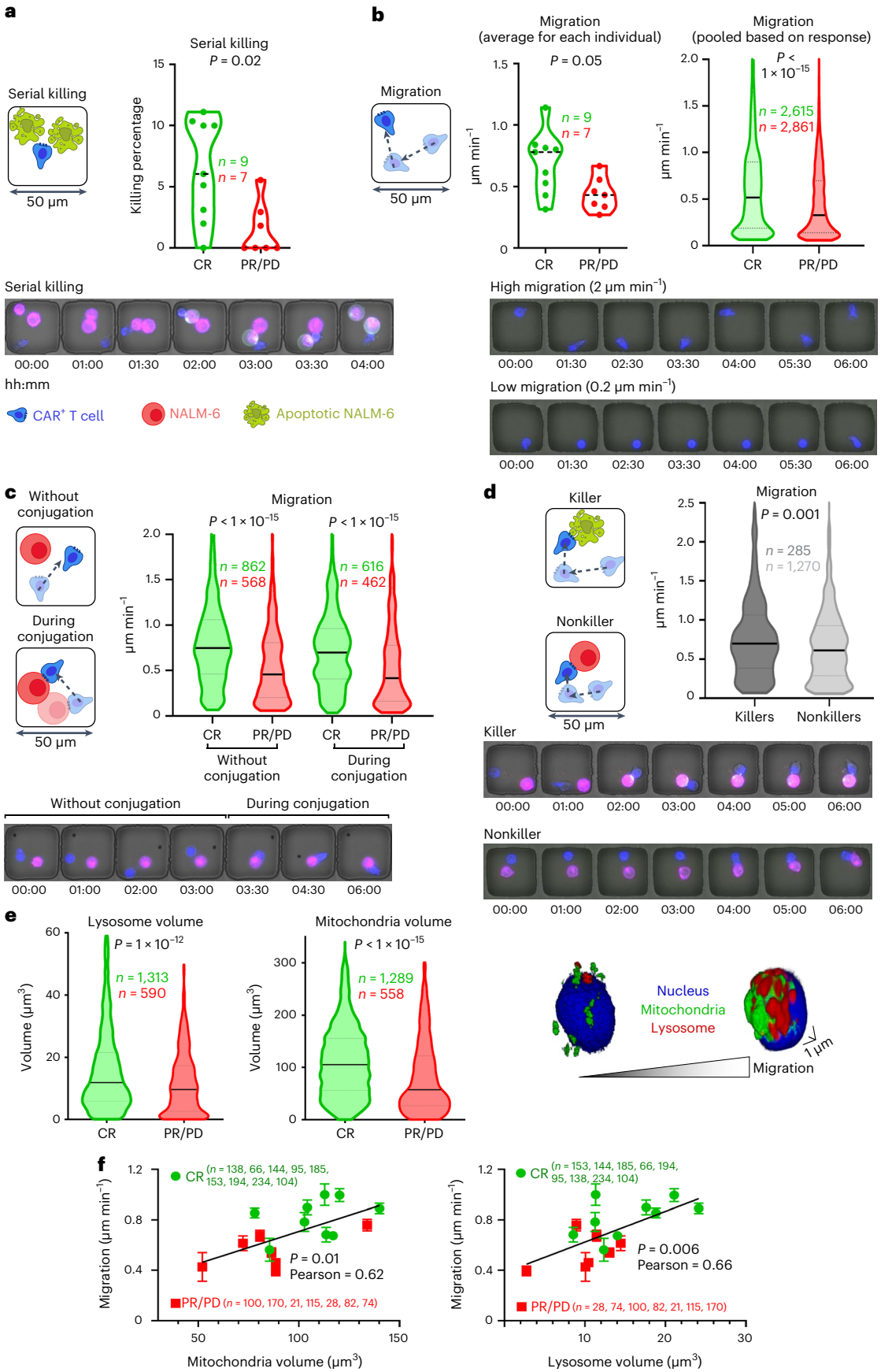

https://doi.org/10.1038/s43018-024-00768-3

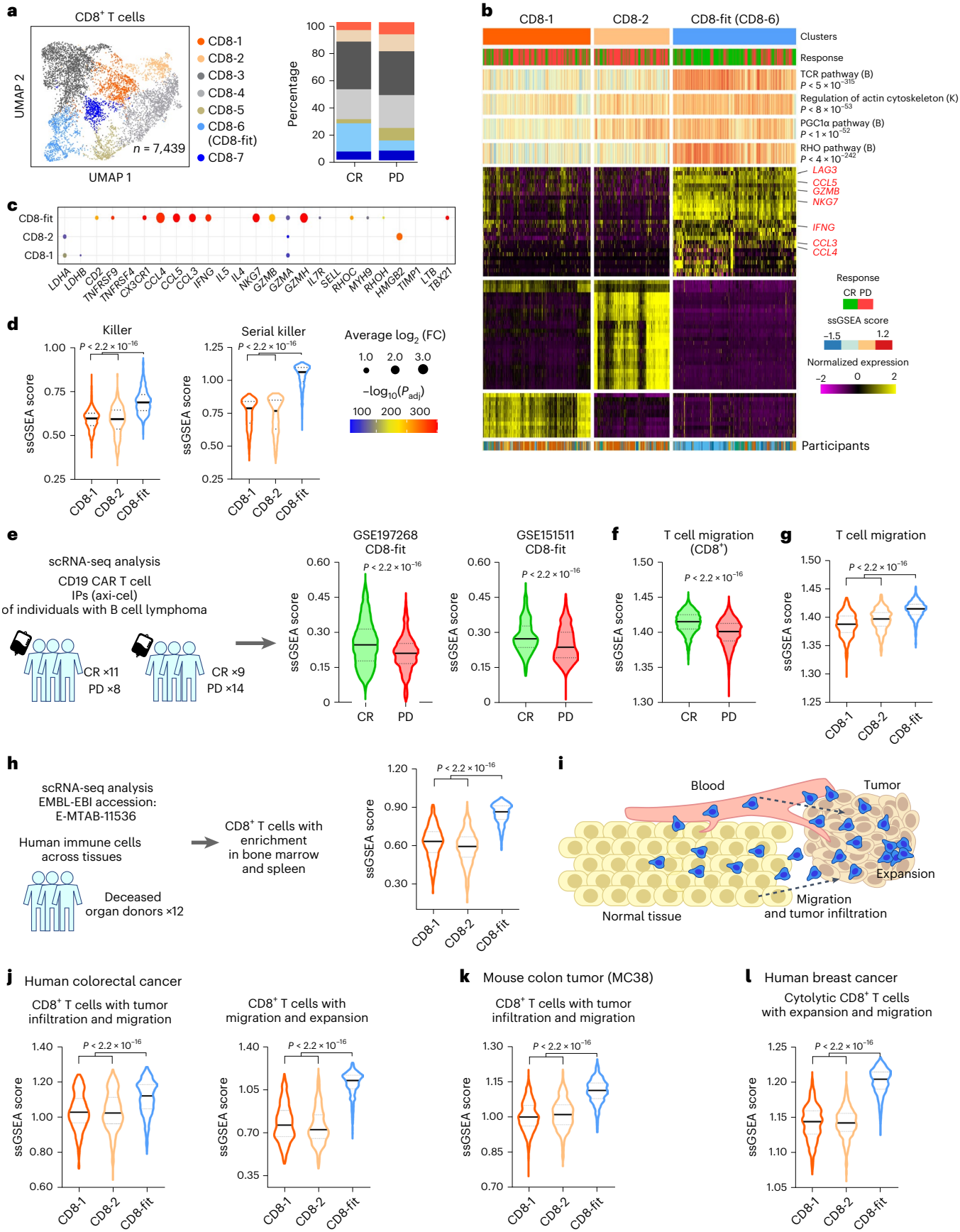

https://doi.org/10.1038/s43018-024-00768-3

Fig. 3 | Molecular profile of CD8-fit T cells, a subset of CAR T cell IPs associated with clinical response revealed by scRNA-seq. a, Uniform manifold approximation and projection (UMAP) for $CD8^+$ T cells ($n = 7{,}439$ cells from nine participant IPs). Seven clusters were identified using unsupervised clustering. **b**, Heat map of three $CD8^+$ T cell clusters generated by unsupervised clustering. A color-coded track on top shows the cells from IPs of individuals with CR (green) and those with PD (red), followed by tracks showing ssGSEA scores of TCR, actin cytoskeleton regulation, PGC1α and RHO pathways, respectively. For the sources of the pathways, B indicates BIOCARTA, and K indicates KEGG. The track below the heat map shows the sample origin for each cell. *P* values were computed using a two-tailed Wilcoxon rank-sum test with Bonferroni correction; R, response; NR, no response. **c**, Bubble plot showing key genes that are differentially expressed among the three $CD8^+$ T clusters. *P* values were computed using a two-tailed Wilcoxon rank-sum test with a Bonferroni correction. **d**, Violin plots showing the ssGSEA score comparison between three $CD8^+$ T cell clusters (CD8-1: $n = 572$ cells; CD8-2: $n = 1{,}031$ cells; CD8-fit: $n = 1{,}253$ cells) with the signatures of killer and multifunctional serial killer T cells; FC, fold change; P_{adj}, adjusted *P* value. **e**, Validation of the association between CD8-fit T cells and clinical responses in independent datasets. ssGSEA-derived CD8-fit T cell scores between $CD8^+$ T cells from individuals with CR and those with PD were computed. **f**, Comparison of the migration scores between $CD8^+$ T cells from individuals with CR and those with PD. **g**, Violin plot showing the ssGSEA score for migration calculated for two clusters enriched in PD (CD8-1 and CD8-2) and one CD8-fit cluster enriched in CR. **h**, Violin plots comparing the similarity between the CD8-fit T cell signature and signatures of T cells that traffic to the bone marrow and spleen from a reference dataset of T cells from 12 organ donors. **i**, Schematic overview showing the parameters defined by STARTRAC analysis. **j**–**l**, Molecular signatures of CD8-fit T cells overlap with the signatures of tumor-resident T cells identified by STARTRAC analysis in three separate studies (CD8-1: $n = 572$ cells; CD8-2: $n = 1{,}031$ cells; CD8-fit: $n = 1{,}253$ cells; Supplementary Table 4). The title of each violin plot corresponds to the cluster with its functional annotation as defined by STARTRAC analysis in the studies. For all violin plots, the black bar represents the median, and the dotted lines denote quartiles. *P* values were computed using a two-tailed Welch's test.

migration score was significantly enriched in the CD8-fit T cell cluster compared to in the CD8-1 and CD8-2 T cell clusters ($P < 2.2 \times 10^{-16}$; Fig. 3g). Similarly, transcripts associated with T cell adhesion, including *ITGB1*, *ITGB2* and *ITM2B*, were significantly enriched in the CD8-fit T cell cluster compared to in the CD8-1 and CD8-2 T cell clusters ($P < 2.2 \times 10^{-16}$; Extended Data Fig. 4). By contrast, none of the genes associated with a migration/exhaustion phenotype, including *CD38*, *MYO7A*, *MYO7B* and *CAV1*, were expressed in these $CD8^+$ T cells regardless of clinical response (Extended Data Fig. 3b)[9,27].

CAR T cells associated with response in lymphoma need to be able to migrate to the lymphoid organs. To validate if CD8-fit T cells shared molecular properties of T cells that migrate to lymphoid organs, we performed comparative assessments of CD8-fit and CD8-1/CD8-2 T cells and showed that the signature of CD8-fit T cells overlaps with the signatures of T cells trafficking to the bone marrow and spleen (Fig. 3h)[28]. To broaden the significance of CD8-fit T cells as a subset of multifunctional tumor-infiltrating $CD8^+$ T cells, we compared the molecular profile of CD8-fit T cells to the signatures of tumor-resident T cells identified by single T cell analysis by RNA-seq and TCR tracking (STARTRAC)[29]. STARTRAC performs paired scRNA-seq and TCR profiling (tracking clonotypes) to identify the properties of T cells that migrate and expand in the tumor relative to paired normal tissue and blood (Fig. 3i). We compared three STARTRAC datasets: (1) 11,138 T cells derived from tumor, adjacent normal tissue and peripheral blood of individuals with colorectal cancer; (2) 64,449 T cells from syngeneic mouse MC38 tumors and (3) 15,831 T cells from the tumor and sentinel lymph nodes of individuals with breast cancer[29–31]. In all three published STARTRAC datasets, CD8-fit marked tumor migrating, cytolytic cells capable of intratumoral expansion, validating the significance of CD8-fit T cells as a subpopulation of multifunctional antitumor T cells (Fig. 3j–l).

Having established CD8-fit T cells as a potent antitumor T cell subset, we next wanted to investigate whether the CD8-fit T cell subset was present within peripheral blood mononuclear cells (PBMCs) before manufacture or whether they develop from the manufacturing process that facilitates the polarization of CD8-fit T cells in select donors. Subsetting $CD8^+$ T cells from healthy donors[32], ssGSEA confirmed that activated $CD8^+$ T cells contain CD8-fit-like T cells (Extended Data Fig. 5a–c), illustrating that CD8-fit T cells are present in healthy donor-derived T cells. We also quantified CD8-fit T cells within PBMCs collected within 30 days before treatment and observed that CD8-fit T cells were significantly enriched in individuals who achieved CR with subsequent CAR T cell treatment[24] (Extended Data Fig. 5d). This result suggests that the CD8-fit T cell population was already enriched within individuals who achieved CR even before manufacture.

We next analyzed $CD4^+$ T cells and first confirmed that $CD4^+$ T cells from individuals who achieved CR showed a significant enrichment in the T cell migration score compared to $CD4^+$ T cells from individuals who were associated with PD (Extended Data Fig. 6a). Analysis of the DEGs and unsupervised clustering of the $CD4^+$ T cells revealed nine clusters, where two clusters (CD4-4 and CD4-1) were predominantly comprised of cells from individuals with PD and CR, respectively (Extended Data Fig. 6b,c). Similar to the $CD8^+$ T cell clusters, genes for immediate cytotoxicity were enriched in the CD4-1 cluster (Extended Data Fig. 6d). In aggregate, scRNA-seq revealed that $CD8^+$ T cells from IPs from individuals with CR are enriched in serial killer cells primed for immediate cytotoxicity, whereas $CD4^+$ T cells from IPs from individuals with CR are associated with signatures of long-term persistence. This divergence in function and long-term in vivo persistence is well supported by other preclinical and recent long-term follow-up clinical data[33,34]. Importantly, integrating the scRNA-seq data with functional single-cell data showed that migration could mark subsets of multifunctional cells primed for clinical efficacy.

Inhibition of AMPK decreases T cell migration and function

As suggested by the scRNA-seq data of the IP T cells, we sought to validate a role for AMPK activation in impacting the migration and functionality of T cells. We used healthy donor-derived CD19-specific CAR^+ human T cells with a CD28 endodomain (designated 19-28z) and inhibited the activity of AMPK in 19-28z T cells using the small-molecule inhibitor dorsomorphin (compound C (CC)). Cells treated with CC (>90% viability) showed profound defects in morphology (aspect

Fig. 4 | Marker-free transwell migration assay enables the enrichment of CD8-fit T cells. a, Modified transwell assay for the isolation of migratory and nonmigratory 19-28z T cells. **b**, Percentages of 19-28z T cells that migrated across the transwell membrane after 4–6 h. The individual points ($n = 5$) represent the percentages for separate transwell experiments from four separate donors (biological replicates), and the error bar shows s.e.m. **c**, UMAP for 16,158 cells from technical replicate experiments for two separate donors. The bar graph on the right shows the distribution of $CD8^+$ T cells from migratory (Mig) and nonmigratory (Unmig) T cells among 12 clusters determined using unsupervised clustering. **d**, Bubble plot showing key genes consistent with CD8-fit T cells (Fig. 2c) among four $CD8^+$ T clusters. *P* values were computed using a two-tailed Wilcoxon rank-sum test with Bonferroni correction. **e**, Violin plots showing the ssGSEA score comparison between migratory and nonmigratory $CD8^+$ T cell clusters with the signatures of CD8-fit T cells, killer T cells, T cell migration and PGC1α regulation. The black bar represents the median, and the dotted lines denote quartiles. *P* values were computed using a two-tailed Welch's test. **f**, Basal oxygen consumption rate (OCR) levels were measured for migratory and nonmigratory 19-28z T cell populations. *P* values were calculated at each time point ($n = 4$ technical replicates) comparing the migratory and nonmigratory subsets using a two-way analysis of variance with a Bonferroni correction; $^{****}P < 1 \times 10^{-15}$. **g**, A confocal 3D image of a migratory 19-28z T cell. The nucleus is shown in blue, and mitochondria are shown in green. The plot on the right shows the number of mitochondria per cell compared between migratory and nonmigratory 19-28z T cells.

https://doi.org/10.1038/s43018-024-00768-3

ratio) and migration, confirming that AMPK activity is essential for the migration of T cells (Extended Data Fig. 7a,b). Consistent with impaired migration, CC-treated 19-28z T cells showed a decreased propensity to conjugate to tumor cells in single-cell assays, showed significantly longer conjugation times, and delayed induction of tumor cell apoptosis compared to untreated 19-28z T cells (Extended Data Fig. 7c–e). We also confirmed that this requirement of AMPK for migration was generalizable to genetically unmodified, tumor-reactive T cells and not just CAR T cells (Extended Data Fig. 7f and Supplementary Video 7).

T cell migration enables enrichment of CD8-fit T cells

Because the integrated single-cell profiling of IP T cells showed that migration could mark subsets of multifunctional cells primed for antitumor function, we wanted to perform proof-of-concept assays to test if selecting for migratory T cells permits the enrichment of

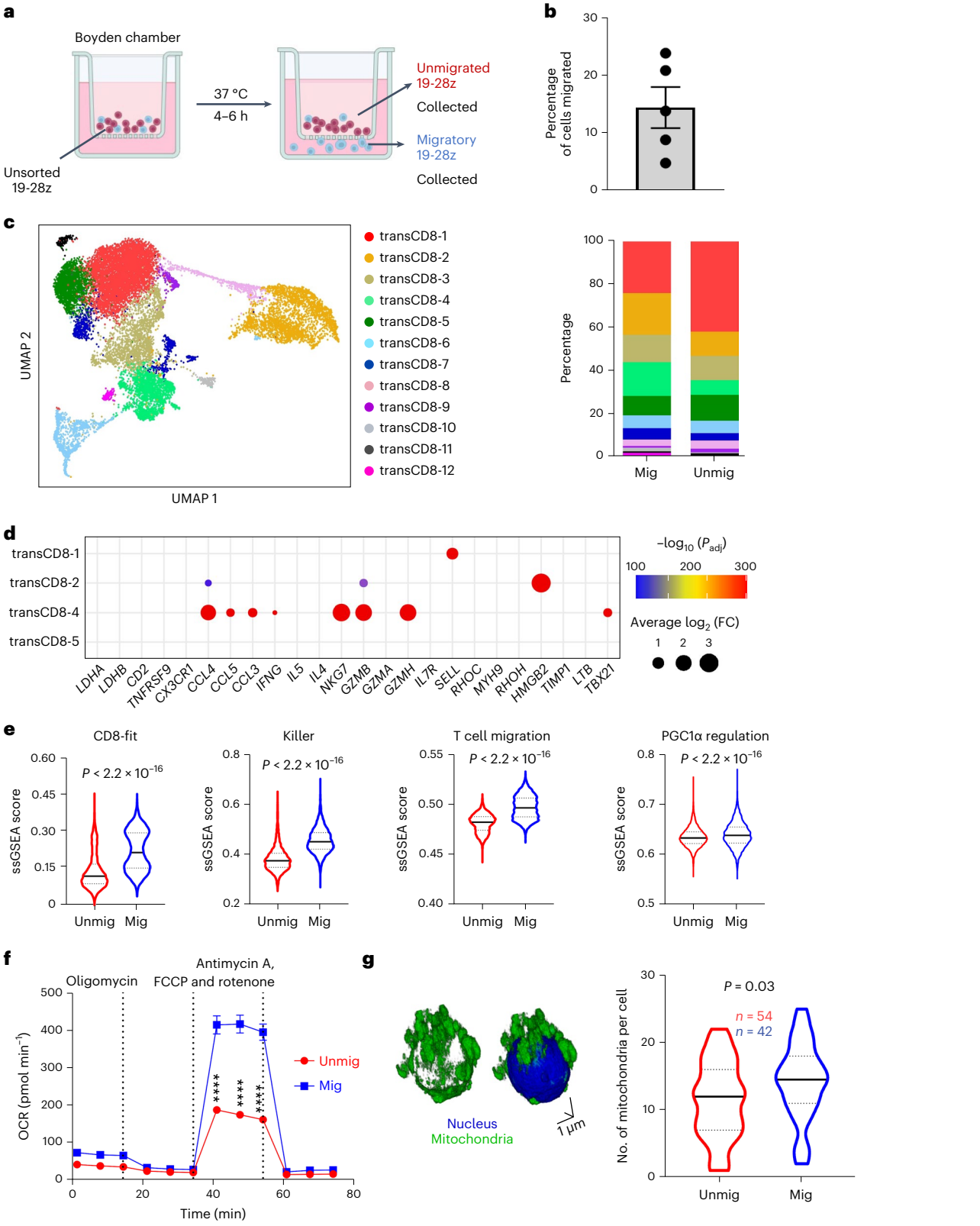

https://doi.org/10.1038/s43018-024-00768-3

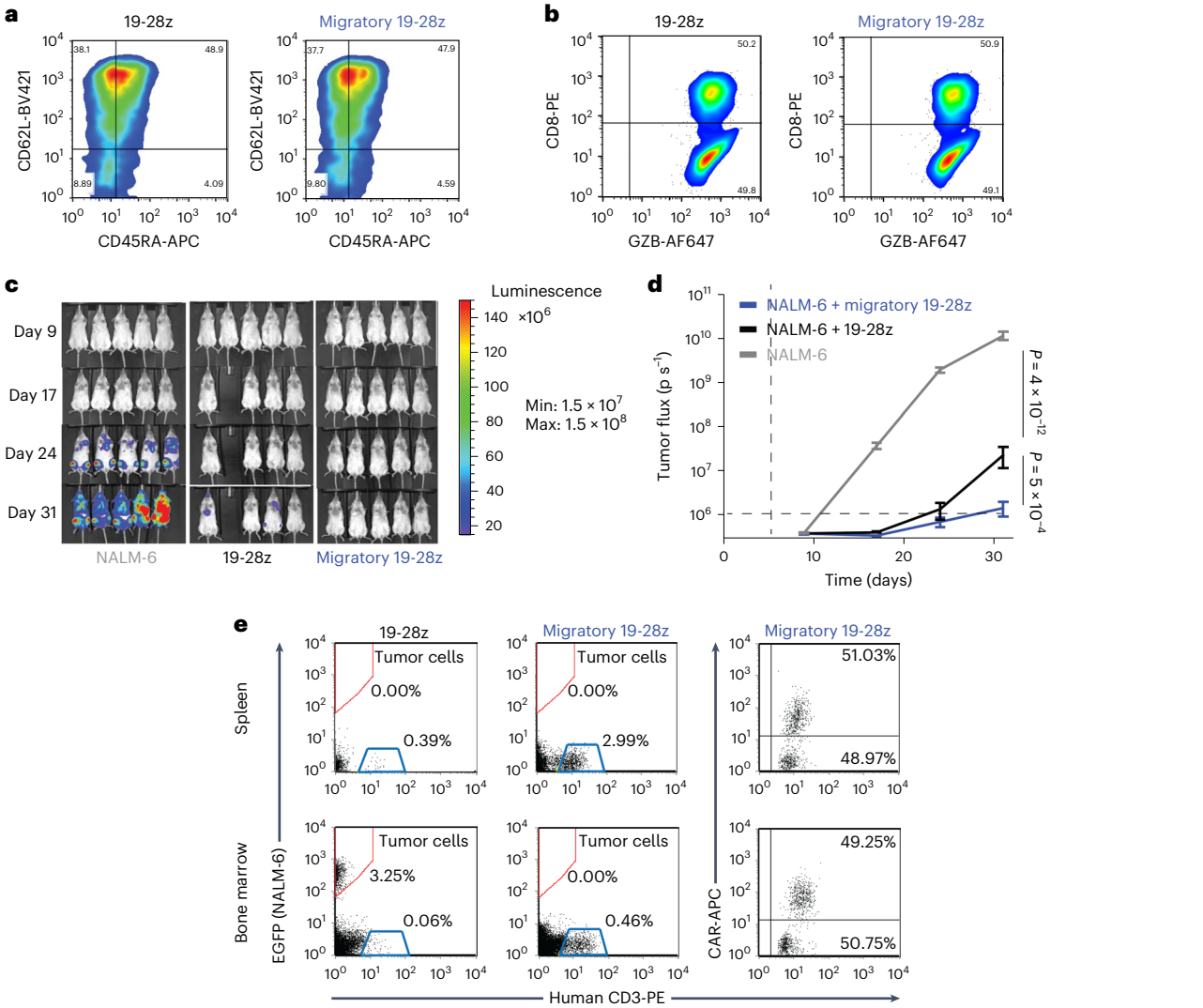

Fig. 5 | Phenotype and in vivo efficacy of migratory CAR T cells. a,**b**, Phenotype (**a**) and granzyme B (GZB) expression (**b**) of migratory and unsorted 19-28z T cells as determined by flow cytometry. **c**, Representative false-colored images illustrating the photon flux from ffLuc-expressing EGFP$^+$ NALM-6 cells. **d**, Time course of the longitudinal measurements of NALM-6-derived photon flux from the three separate cohorts of mice ($n = 10$ mice in each group). Representative data from two independent experiments are shown. Background luminescence was defined based on mice with no tumor. Error bars represent s.e.m., and *P* values were computed using a two-tailed Mann–Whitney test. **e**, On day 31, four mice from each group were killed, and tissues (bone marrow and spleen) were collected and analyzed by flow cytometry for the expression of human CD3 (human T cells) and enhanced green fluorescent protein (EGFP; gated within human CD19$^+$ cells). The flow data are representative of one mouse in each group.

CD8-fit T cells. Because the molecules that define CD8-fit T cells are predominantly associated with function rather than phenotype, protein marker-based sorting was not feasible. To solve this issue, we used a modified transwell assay with pore sizes (5 µm) consistent with previously published confinement studies of T cells in vitro to directly sort migratory cells[35]. The 19-28z T cells were seeded onto a Boyden chamber, and migratory T cells were collected from the bottom chamber and compared to nonmigratory T cells collected from the top chamber (Fig. 4a). Across multiple donor-derived 19-28z T cells, the frequency of migratory cells varied from 5 to 24% (Fig. 4b). We performed scRNA-seq to compare the transcriptional profiles of the 19-28z migratory and nonmigratory T cells, identified the DEGs between CD8$^+$ T cells from the two populations and performed unsupervised clustering based on the DEGs to identify 12 clusters (Fig. 4c). Clusters transCD8-1 and transCD8-2 were comprised predominantly of nonmigratory 19-28z T cells, whereas clusters transCD8-4 and transCD8-5 were predominantly comprised of migratory 19-28z T cells (Fig. 4c,d). Consistent with the molecular profile of CD8-fit T cells within the IPs, T cells within the transCD8-4 cluster showed high expression of genes associated with effector functionality, including cytotoxicity (*GZMB*, *GZMH* and *NKG7*) and cytokines and chemokines (*CCL3-5* and *IFNG*; Fig. 4d). Using ssGSEA, we confirmed that the migrated 19-28z T cells were enriched in CD8-fit T cells, killer T cells, migratory T cells and T cells with increased PGC1α activity and mitochondrial biogenesis compared to nonmigratory 19-28z T cells (Fig. 4e).

To validate the link between migration and metabolism, we measured the oxygen consumption rate of both the migratory and nonmigratory T cell populations. Metabolic flux analyses revealed that the migratory populations had both higher maximal respiratory capacity and spare respiratory capacity than nonmigratory T cell populations (Fig. 4f). Because the data from IPs suggested differences in mitochondrial volume, we used 3D single-cell confocal microscopy to study mitochondrial structure. Imaging of single cells confirmed that migratory 19-28z T cells had increased mitochondrial volume and an increased number of punctate mitochondria compared to nonmigratory 19-28z T cells (Fig. 4g). Collectively, these scRNA-seq and metabolic profiling

https://doi.org/10.1038/s43018-024-00768-3

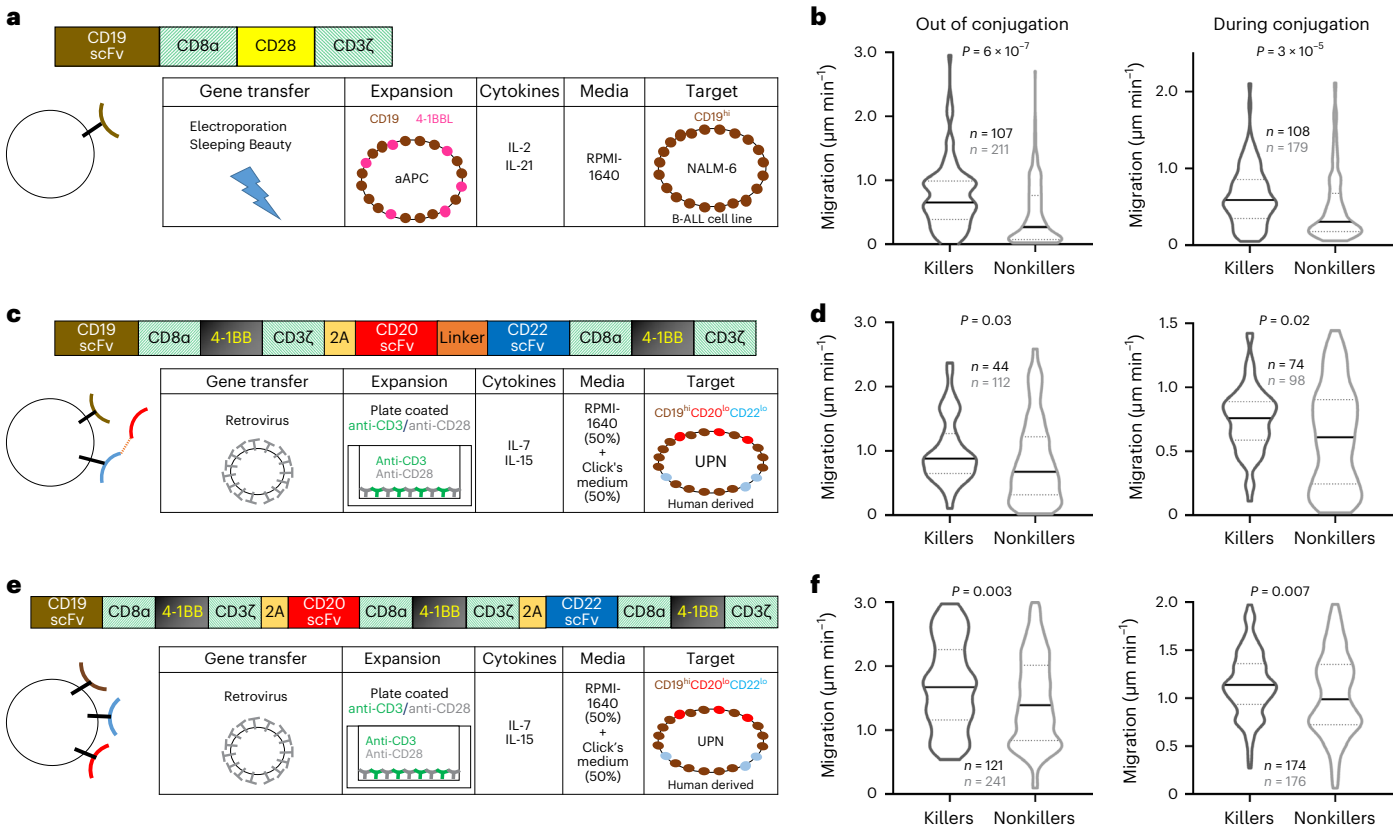

Fig. 6 | Quantifying the link between migration and functionality in diverse CARs. a,**c**,**e**, Schematic illustrating the CAR structure, manufacturing and expansion and the target cells used for profiling functionality of individual CAR T cells using TIMING; B-ALL, B cell acute lymphoblastic leukemia. **b**,**d**,**f**, Migration of individual killer and nonkiller CAR T cells with or without conjugation to tumor cells. All data are from an E:T ratio of 1:1. The black bar represents the median, and the dotted lines denote quartiles. All *P* values were computed using two-tailed Mann–Whitney tests, and each data point (*n*) represents a single effector cell.

data confirmed that a simple transwell migration assay enabled the enrichment of multifunctional CD8-fit T cells.

T cell migration can select cells with antitumor efficacy

Because the scRNA-seq data confirmed the ability of transwell assays to enrich CD8-fit T cells, we next evaluated if transwell assays can enable the isolation of T cells with superior antitumor efficacy. We compared the efficacy of migratory cells to unsorted 19-28z T cells to benchmark their superiority. After transwell sorting, TIMING confirmed that migratory 19-28z T cells harbored a high frequency of T cells with basal migration compared to unsorted 19-28z T cells (Extended Data Fig. 8a).

Consistent with the scRNA-seq data, TIMING assays with NALM-6 tumor cells confirmed that migratory cells were functionally superior cells and were more potent killers (Extended Data Fig. 8b,c). To test if the differences in migration and functional properties of migratory T cells could be explained by their phenotype, we compared the memory phenotype of migratory and unsorted T cells and observed that both populations were comprised predominantly of naive-like ($CD62L^+CD45RA^+$) and central memory ($CD62L^-CD45RA^+$) CAR T cells (Fig. 5a). Both migratory and unsorted populations showed no difference in the expression of CAR (Extended Data Fig. 8d), intracellular granzyme B (Fig. 5b) or the $CD4^+$:$CD8^+$ T cell ratio (Extended Data Fig. 8d), consistent with transcriptional and functional data from IP profiling between clinical responses.

We assessed the efficacy of the migratory 19-28z T cell population using a model of established leukemia (Extended Data Fig. 9a). Migratory 19-28z T cells demonstrated potent and superior antitumor activity, reducing tumor burden to the detection limit, with tumor flux significantly lower than in unsorted 19-28z T cells (Fig. 5c,d). It is worth emphasizing that this improvement in efficacy was obtained purely by isolation of the subpopulation of migratory cells in the population without any additional culturing or modifications. In both the bone marrow and spleen, mice treated with migratory 19-28z T cells harbored no tumor cells but only persisting CAR T cells, and this was different from mice treated with unsorted 19-28z T cells (Fig. 5e). In an independent experiment, we compared the efficacy of migratory and unsorted 19-28z T cells at suboptimal doses against these same NALM-6 tumors in vivo. Migratory 19-28z T cells showed enhanced antitumor activity compared to unsorted 19-28z T cells (Extended Data Fig. 9b,c). In aggregate, these results demonstrate that migration is a desired feature indicative of subpopulations of T cells with optimal function and in vivo persistence.

Killer T cells show better migration than nonkiller cells

We next tested if the link between killing and migration is generalizable to CD19-specific CAR T cells derived from diverse manufacturing protocols and against multiple tumor targets. Accordingly, we used TIMING to first compare the migration of killer and nonkiller CAR T cells electroporated and manufactured with a CD19-specific CAR containing the CD8 hinge and transmembrane regions (19-8-28z; Fig. 6a). Consistent with our other data, individual killer 19-8-28z T cells demonstrated higher migration both with or without conjugation to NALM-6 tumor cells than nonkiller 19-8-28z T cells (Fig. 6b and Extended Data Fig. 10a). Next, we tested two tri-specific CAR T cells designed for mitigating CD19 escape in primary acute lymphocytic leukemia[36]. These tri-specific CAR T cells were retrovirally transduced, the CAR design incorporated a 41BB endodomain, and the T cells were expanded by treating with anti-CD3, anti-CD28, interleukin-7 (IL-7) and IL-15, as

described previously[37]. We tested these T cells against human-derived tumor cells. Again, by comparisons using TIMING, individual killer CAR T cells demonstrated higher migration both with and without conjugation to human-derived tumor cell lines than nonkiller CAR T cells (Fig. 6c–f and Extended Data Fig. 10b,c). These data suggest that the link between migration and killing can be preserved across multiple CAR designs and manufacturing protocols.

Discussion

With the approval of CD19-specific CAR T cells as living drugs, there is a need to define biomarkers that provide insights into the clinical impact of adoptive immunotherapy. Identifying cellular properties associated with clinical efficacy are important for ensuring predictable clinical outcomes and for defining desirable attributes during biomanufacturing. Prior studies of IPs have been limited to static profiling based on flow cytometry[38], whole-transcriptome profiling[8,38] or cytokine secretion[7], but our dataset is a multiomics profile that integrates dynamic imaging across thousands of T cells and their interactions with tumor cells. Our multimodal single-cell integration identified that a potent multifunctional subset of CD8$^+$ T cells, CD8-fit T cells, is endowed with both migration and serial killing.

How do CD8-fit T cells compare to conventional subsets of CD8$^+$ T cells? CD8-fit T cells are a hybrid T cell subset that share features of effector memory T cells (for example, *GZMB*, *PRF1*, *IFNG*, *GZMK* and *TBX21* expression) and natural killer cell receptor-enriched T cells (for example, *NKG7*, *KLRG1* and *KLRK1* expression) but not signatures of exhaustion (for example, *TOX*, *PDCD1*, *ID2* and *HAVCR2* expression)[18]. As we have described, the lack of exhaustion was functionally validated by integrating the molecular signatures with serial killing at single-cell resolution (Fig. 3d). CD8-fit T cells are also uniquely characterized by the high expression of *GZMH* (or in mice *Gzmc*), a gene that encodes a nonredundant granzyme that cleaves orthogonal mitochondrial and nuclear target proteins compared to granzyme B[39]. Although these molecular properties listed above are characteristic of differentiated CD8$^+$ T cell subsets, CD8-fit T cells deviate from these more differentiated subsets and are characterized by signatures of the *TCF7* regulon[23], *HOPX* (the transcription cofactor of pre-effector T cells[40]) and PGC1α-mediated mitochondrial biogenesis[41]. CD8-fit T cells are thus a unique subset with overlapping properties of early- and late-differentiation memory CD8$^+$ T cells.

The discovery of CD8-fit T cells translationally advances the results from independent preclinical studies using two-photon microscopy that demonstrated (1) mouse T cell migration before engagement and killing of tumor cells is an essential component of their efficacy[42,43], (2) both CD4$^+$ and CD8$^+$ CAR T cells mediate direct and indirect cytotoxicity after migration to tumors[44], (3) migratory T cells are long-duration tumor-resident T cells[27], (4) functional exhaustion by PD-1 induces T cell migration paralysis and blockade of PD-1 can restore T cell migration and function[45], and (5) T cell migration in tissues increases with serial killing and tumor rejection[46]. This ability of intrinsic T cell migration to promote tumor exploration is a central feature of cells as drugs that distinguishes them from small-molecule and protein therapeutics[47]. At the molecular level, the genes/proteins involved in migration, including *RHOA*, *RAC1* and *CDC42*, affect multiple aspects of T cell immunobiology, including cell polarity, chemotaxis, synapse formation, signaling and effector responses, and, hence, it is not surprising that migration is a biomarker for cells with optimal effector functionality[48].

T cells exhibiting migration have a high bioenergetic requirement to support locomotion. Our results confirmed that the migratory CAR T cells had enhanced mitochondrial spare respiratory capacity, a property that likely promotes long-term survival[49,50]. Three-dimensional confocal microscopy also demonstrated increased punctate mitochondria in individual cells with migration. Within this context, we confirmed that inhibiting AMPK, the master regulator of mitochondrial remodeling, has a profound impact on T cell migration and consequently function at the single-cell level. AMPK, via phosphorylation of folliculin-interacting protein 1, induces the nuclear translocation of transcription factor EB, which in turn increases the expression of not only PGC1α but also genes responsible for lysosomal biogenesis[21]. This sets the stage for additional studies that explore the link between AMPK (using knockdown or knockout studies) as a modulator of energetics and function within individual T cells and their antitumor efficacy. AMPK is a global modulator of many different aspects of cell biology that need to be mapped within the context of T cells[51,52].

There are limitations to our study. Although our discovery cohort was limited to IPs from 16 individuals, we validated the importance of CD8-fit T cells in IPs from other cohorts and have demonstrated that CD8-fit T cells share molecular signatures of T cells that longitudinally persist in individuals after treatment with CAR T cells. In the current manuscript, our focus was on maximizing the assays that we could perform with the residual cells recovered from the infusion bag ($<5 \times 10^5$ cells); we studied them using TIMING, confocal microscopy and scRNA-seq. We recognize that the two-dimensional (2D) platform with TIMING is not the perfect method to model 3D T cell migration and that CAR T cell migration in 2D (~1 μm min^{-1}) is slower than 3D migration in vivo (~6 μm min^{-1}, two-photon microscopy)[53]. We also emphasize that while 2D migration is one of the parameters reported by our TIMING assay, it is sample sparing (most assays reported here used 2×10^5 cells or less), thus allowing us to perform confocal imaging on the same IPs. Furthermore, TIMING allows profiling of serial killing (shown to be different between responders and nonresponders (CR and PR/PD); Fig. 2a), and the kinetics of killing mapped to migration at the single-cell level. The discovery of 2D migration as a biomarker for T cell function sets the stage for us to map the role of 3D T cell migration with other IP products in the future when cells are not limiting[54].

In summary, we have identified the transcriptional features of CD8-fit T cells with validated single-cell functional potential and antitumor efficacy. We anticipate that the availability of a defined molecular signature of efficacy will allow the engineering, manufacture and translation of potent T cell-based therapies, leading to predictable and durable clinical outcomes.

Methods

Human studies statement

All work outlined in this report was performed according to protocols approved by the Institutional Review Boards at the University of Houston and the University of Texas MD Anderson Cancer Center. Axi-cel IPs were administered as standard of care, and participants provided written informed consent. Human blood donors for primary T cell isolation provided written informed consent through the Gulf Coast Regional Blood Center. Tumor-infiltrating lymphocytes referenced in Extended Data Fig. 7f were expanded from surgical resection tissue under protocol number 2004–0069 approved by the Institutional Review Board of the University of Texas MD Anderson Cancer Center and an FDA-approved Investigational New Drug application (NCT00338377).

Animal studies statement

All animal experiments performed in this study were approved and were performed in compliance with the Institutional Animal Care and Use Committee at the University of Houston. The limit for maximal tumor size was 2,000 mm^3 according to Institutional Animal Care and Use Committee guidelines, and the limit was not exceeded for this study.

Human samples

Participants with DLBCL were treated with anti-CD19 CAR T cells. T cells from the participants were originally isolated through leukapheresis and sent to the Kite Pharma manufacturing facility. The facility engineered the T cells to express CD28 and CD3ζ endodomains and shipped the cells back to the respective physicians. After CAR T cell infusion,

leftover cells in infusion bags were collected and transferred to the laboratory for microscopy assays and scRNA-seq. At the 6-month follow-up, nine individuals showed CR (56%), one showed PR (6%), and six showed PD (38%).

Cell lines and primary T cells

The human pre-B cell leukemic cell line NALM-6 (ATCC, CRL-3273) was cultured in T cell medium (RPMI + 10% fetal bovine serum (FBS)) and used as $CD19^+$ target cells. Human T cells were isolated from whole blood. Second-generation CAR signaling via CD28 and CD3ζ endodomains (with a mutated IgG4 spacer) was expressed in human T cells by electroporation with DNA plasmids from the Sleeping Beauty transposon/transposase system, as described previously[11]. T cells were used 2–3 weeks after transfection.

Nanowell array fabrication

Nanowell array fabrication to investigate effector functions at the single-cell level was performed as described previously[55,56]. Briefly, we designed a master template nanowell array using AutoCAD (Autodesk) and fabricated it on a silicon wafer using soft lithography techniques. We made the nanowell array by pouring PDMS on the silicon wafer and spinning the silicon wafer using a spin coater, followed by baking it at 70 °C for 2 h. We then plasma oxidized the nanowell and attached it to the bottom of a 50-mm glass-bottom Petri dish. The nanogrid contains approximately 5,000 wells, and each well was 50 µm × 50 µm × 50 µm in size.

TIMING assays to profile functionality at the single-cell level

We labeled approximately 0.5 million–1 million CAR T cells with PKH67 green fluorescent dye (Sigma) and 1 million NALM-6 cells with PKH26 red fluorescent dye (Sigma), as per the manufacturer's protocol. We loaded both CAR T cells and NALM-6 cells on a nanowell array in a way to reach mainly one effector cell and one to two target cells per nanowell (E:T = 1:1 or 1:2). We used complete cell culture medium (IMDM + 10% FBS) to cover the nanowell array and added Annexin V-Alexa Fluor 647 (Invitrogen) to the covering medium to detect cell apoptosis during the experiment.

We used an inverted fluorescence microscope (Zeiss) that was equipped with a Lambda-DG4 illumination system, differential interference contrast condenser annulus, ×20/0.80-NA Zeiss Plan-Apochromat objective and Orca Flash 4.0 camera (Hamamatsu). We placed the Petri dish containing the PDMS nanowell array on a motorized stage in a box to maintain the temperature at 37 °C and CO_2 level at 5% and used Alexa Fluor (488 nm), TexasRed (566 nm) and Cy5 (651 nm) filters for the detection of CAR T cells, NALM-6 cells and apoptosis, respectively. Images were acquired for 6 h with 5-min intervals.

Confocal microscopy for integrated measurements of subcellular organelles

For confocal microscopy, we fluorescently labeled ~300,000 CAR T cells at 37 °C for 30 min in a 1:1 (vol/vol) solution of live-cell staining buffer (Abcam) and RPMI-1640 (Corning) containing final concentrations of 500 nM MitoTracker Deep Red (Invitrogen), 250 nM LysoRed (Abcam) and 1 µM Hoechst 33342 (Sigma) for labeling mitochondria, lysosomes and nuclei, respectively. We then washed cells with Hanks' balanced salt solution (Cellgro) + 10% HEPES (Corning), resuspended the cells in cell culture medium (RPMI + 10% FBS) and loaded labeled cells on a glass-bottom 96-well plate (MatTek Corporation) for confocal imaging.

We used a Nikon A1/TiE inverted microscope equipped with a ×100/1.45-NA objective for imaging. Specifically, we acquired 3D images (~50 slices, 0.3 µm per slice) from multiple fields of view using DAPI (404.0 nm), FITC (488.0 nm), TexasRed (561.8 nm) and Cy5 (641.0 nm) filters for the detection of nuclei, membranes, lysosomes and mitochondria, respectively.

Image processing, cell segmentation, cell tracking and data analytics

For TIMING assay image processing, we used a homemade pipeline to analyze 16-bit images as described previously[57]. Briefly, an automated pipeline was implemented for automatic detection of nanowells, cell segmentation, tracking and feature computation. The pipeline output are tables containing statistical information for nanowells with one effector cell and up to five target cells (1:1 E:T–1:5 E:T). We partitioned events based on the functionalities of the cells, that is, 1:1 E:T killing, monokilling and serial killing (Extended Data Fig. 2a,b):

(1) 1:1 E:T killing: a single T cell killing a target cell existing in the nanowell after conjugation.
(2) Monokilling: a single T cell killing only one target cell after conjugation, while multiple targets (at least two) exist in the nanowell.
(3) Serial killing: a single T cell killing at least two target cells after conjugation, while multiple targets (at least two) exist in the nanowell.
(4) No killing: T cells without killing any target cells despite evidence of conjugation.

For tracking mitochondria and lysosomes within cells using confocal microscopy, *z* stacks of 16-bit images were extracted for each channel and processed in ImageJ (National Institutes of Health) using a series of plugins. First, the Subtract Background plugin was applied to the mitochondria and lysosome channels before segmentation to reduce variations in background intensities. Next, the 3D Objects Counter plugin was applied to the background-corrected image to determine mitochondrial and lysosome regions of interest. Regions of interest were overlaid onto the original image, and measurements were collected. Similarly, the 3D Objects Counter plugin was used on the nucleus channel using the original image only. Last, tracking of single-cell movement was performed using the TrackMate plugin[58] to filter out unstable cells after their movement. All measurements were consolidated in R, where mitochondria and nuclei were matched to their corresponding cell.

scRNA-seq

We performed scRNA-seq on nine samples (four CR and five PD) with enough numbers of residual cells. We first used a dead cell removal kit (Miltenyi Biotec) containing microbeads for the magnetic labeling of dead cells, and we removed dead cells by passing the resuspended cells through the magnetic field of a MACS separator. Library preparation was performed in three batches. For each batch, we used three different TotalSeq C anti-human Hashtag Antibodies (BioLegend) to multiplex the samples as per the manufacturer's protocols. We then performed transcriptome and TCR capturing using the 10x Chromium platform (10x Genomics) and used a Chromium Single Cell 5′ reagent v2 kit for gene expression and V(D)J profiling. Sequencing was performed using a HiSeq PE150 sequencer (Illumina). Library preparation from the transwell experiments was performed without hashing.

scRNA-seq analysis

We processed gene expression FASTQ files generated on an Illumina sequencer using the Cell Ranger pipeline (version 6.0.0, 10x Genomics) for read alignment and generation of feature barcode matrices. The output files were then uploaded into R (version 4.0.1) for further processing using Seurat (version 4.1.0)[59]. We used the SAVER package[60] for data imputation and filtered out the cells with high mitochondrial gene expression (more than 15% of the read counts). For the IPs, we obtained 21,469 cells from nine individuals with a mean number of unique molecular identifiers of 7,738, and from the transwell cohorts, we obtained 23,319 cells from two donors with a mean number of unique molecular identifiers of 7,700.

We detected the highly variable genes and principal components following the Seurat standard workflow for unsupervised clustering of cells and used UMAP for visualization of the clusters. We identified $CD8^+$ and $CD4^+$ T cell subsets using *CD8A*, *CD8B*, *CD4* and *CD40LG* gene markers and identified CAR^+ cells by detection of the CAR sequence (FMC63-CD19scFV, GenBank HM852952.1).

We used the gene set variation analysis (GSVA) package[61] in R to calculate ssGSEA scores for different pathways and predefined gene sets from the Molecular Signatures Database (MSigDB, v7.5.1) for pathway analysis. We also used customized gene sets (TCF7.regulon[23], T cell migration[26] and $CD4^+$ Ki67 (ref. 34)) based on previous publications. Lowly expressed genes (average expression of <0.25) were removed from the pathway analysis. We generated heat maps using the pheatmap package in R. For the pseudotime trajectory analysis, we used the Monocle package in R.

For evaluating the signatures of persistence of $CD8^+$ T cells, we obtained gene expression and TCR sequences from the dbGaP database under dbGaP study accession phs002966.v1.p1. We calculated transcriptomic prediction scores using Seurat and used GSEA software to make the enrichment plot. We performed statistical analysis and generated *P* values in R.

Migration of T cells through a transwell migration chamber

Unstimulated, overnight serum-deprived CAR T cells were seeded on the top compartment of a PET 5-µm-pore Boyden transwell migration chamber (EMD Millipore), while the lower compartment contained FBS-rich medium. After 4–6 h, the cells from the bottom and the top compartments were collected as 'migratory' and 'nonmigratory' populations, respectively. The lower part of the membrane was washed into the migratory cell suspension, while the top surface of the membrane was washed into the nonmigratory cell suspension. We analyzed the phenotype and function of the cells using flow cytometry, TIMING, confocal microscopy and scRNA-seq.

Flow cytometry-based phenotyping

For phenotyping, we stained CAR T cells using a panel of human-specific antibodies, including CD62L (DREG-56), CD45RA (HI100), CD3 (SK7), CD4 (OKT4), CD8 (RPA-T8) and CD19 (HIB-19), and intracellular staining using granzyme B (QA16A02) from Biolegend. The anti-CAR scFv was made in-house[62]. We analyzed the cells using a BD LSRFortessa X-20 cell analyzer.

CC inhibition assays

We incubated T cells with 10 µM dorsomorphin (Sigma-Aldrich) for a period of 6–24 h. The T cells were subsequently used for either migration assays or functional profiling using TIMING assays. Incubation with CC did not have an impact on T cell viability.

In vivo efficacy of CAR T cells

On day 0, 7-week-old NOD.Cg-*Prkdc*^{scid}*Il2rg*^{tm1wjl}/SzJ female mice (Charles River) were injected intravenously via the tail vein with 1.5×10^4 $EGFP^+ffLuc^+$ NALM-6 cells. Mice ($n = 10$ per group) in the two treatment cohorts received 10^7 CAR T cells on day 5 via tail vein injection. One group of mice ($n = 10$) bearing tumors was not treated with T cells. Anesthetized mice underwent bioluminescent imaging in an anterior–posterior position using a Xenogen IVIS 100 series system (Caliper Life Sciences) 10 min after subcutaneous injection (at the neck and shoulder) with 150 µl (200 µg per mouse) of freshly thawed aqueous solution of D-luciferin potassium salt (Caliper Life Sciences), as previously described[63]. Photons emitted from NALM-6 xenografts were serially quantified using the Living Image 2.50.1 (Caliper Life Sciences) program. On day 28, five mice in each group were killed to evaluate the presence of T cells and tumor cells. Bone marrow was flushed from the femurs using 30-gauge × 1.3-cm needles (BD, 305106) with 2% FBS in PBS. Spleens in 2% FBS/PBS were disrupted using a syringe and passed through a 40-µm nylon cell strainer (BD, 352340) to obtain a single-cell suspension. Red blood cells from bone marrow, spleen and peripheral blood were lysed using ACK lysing buffer (Gibco-Invitrogen, A10492), and remaining cells were stained for the presence of tumor (human CD19 and EGFP), T cells (human CD3) and CAR T cells (scFv) by flow cytometry. The remaining five mice in each group were used to determine the survival curves. In the suboptimal dose model, the mice were treated exactly as above except that on day 5, 2×10^6 CAR T cells were injected intravenously.

Data visualization

Data plotting and statistical analyses were performed in R and GraphPad Prism v7. Schematics were made using Microsoft PowerPoint and Biorender via full license. Figure panels were made in Inkscape (v1.1.2).

Statistics and reproducibility

No statistical methods were used to predetermine sample sizes for the IPs or animal studies. Animal studies were randomized. The researchers were not blinded to allocation during experiments and outcome assessment. Data collection and analysis were not performed blind to the conditions of the experiments. No data were excluded from the analysis except for TIMING results. Time of conjugation and time of death events lower than 10 min were omitted from analysis. Time of conjugation lower than 10 min assumes no synapse formation, and time of death lower than 10 min can be attributed to spontaneous cell death. Data distribution was assumed to have unequal variance, but this was not formally tested. Further information on research design is available in the Nature Research Reporting Summary linked to this article

Reporting summary

Further information on research design is available in the Nature Portfolio Reporting Summary linked to this article.

Data availability

The scRNA-seq data of the IPs are available under GEO accession number GSE208052, and migratory CAR T cell scRNA-seq data are available under GEO accession number GSE253872. External datasets used for CD8-fit T cell signature validation were accessed under GEO accession numbers GSE197268 (ref. 24) and GSE151511 (ref. 8) and EMBL-EBI accession number E-MTAB-11536 (ref. 28). The external dataset used for T cell persistence was accessed via dbGaP under study accession phs002966.v1.p1 (ref. 25). The healthy donor T cell scRNA-seq data were accessed under accession number GSE201035 (ref. 32). Source data are provided with this paper. All other data supporting the findings of this study are available from the corresponding author on reasonable request.

Code availability

All relevant package and software information is provided in the Methods. No custom code was generated in the course of this study.

References

1. Rosenberg, S. A. et al. Durable complete responses in heavily pretreated patients with metastatic melanoma using T-cell transfer immunotherapy. *Clin. Cancer Res.* **17**, 4550–4557 (2011).
2. Maus, M. V. & June, C. H. Making better chimeric antigen receptors for adoptive T-cell therapy. *Clin. Cancer Res.* **22**, 1875–1884 (2016).
3. Jackson, H. J., Rafiq, S. & Brentjens, R. J. Driving CAR T-cells forward. *Nat. Rev. Clin. Oncol.* **13**, 370–383 (2016).
4. June, C. H., Riddell, S. R. & Schumacher, T. N. Adoptive cellular therapy: a race to the finish line. *Sci. Transl. Med.* **7**, 280ps287 (2015).
5. Park, J. H., Geyer, M. B. & Brentjens, R. J. CD19-targeted CAR T-cell therapeutics for hematologic malignancies: interpreting clinical outcomes to date. *Blood* **127**, 3312–3320 (2016).

6. Sadelain, M., Riviere, I. & Riddell, S. Therapeutic T cell engineering. *Nature* **545**, 423–431 (2017).
7. Rossi, J. et al. Preinfusion polyfunctional anti-CD19 chimeric antigen receptor T cells are associated with clinical outcomes in NHL. *Blood* **132**, 804–814 (2018).
8. Deng, Q. et al. Characteristics of anti-CD19 CAR T cell infusion products associated with efficacy and toxicity in patients with large B cell lymphomas. *Nat. Med.* **26**, 1878–1887 (2020).
9. Romain, G. et al. Multidimensional single-cell analysis identifies a role for CD2–CD58 interactions in clinical antitumor T cell responses. *J. Clin. Invest.* **132**, e159402 (2022).
10. Sabatino, M. et al. Generation of clinical-grade CD19-specific CAR-modified $CD8^+$ memory stem cells for the treatment of human B-cell malignancies. *Blood* **128**, 519–528 (2016).
11. Singh, N., Perazzelli, J., Grupp, S. A. & Barrett, D. M. Early memory phenotypes drive T cell proliferation in patients with pediatric malignancies. *Sci. Transl. Med.* **8**, 320ra323 (2016).
12. Klebanoff, C. A. et al. Determinants of successful $CD8^+$ T-cell adoptive immunotherapy for large established tumors in mice. *Clin. Cancer Res.* **17**, 5343–5352 (2011).
13. Cherkassky, L. et al. Human CAR T cells with cell-intrinsic PD-1 checkpoint blockade resist tumor-mediated inhibition. *J. Clin. Invest.* **126**, 3130–3144 (2016).
14. Textor, A. et al. Efficacy of CAR T-cell therapy in large tumors relies upon stromal targeting by IFNλ. *Cancer Res.* **74**, 6796–6805 (2014).
15. Tschumi, B. O. et al. CART cells are prone to Fas- and DR5-mediated cell death. *J. Immunother. Cancer* **6**, 71 (2018).
16. Huan, T. et al. Activation-induced cell death in CAR-T cell therapy. *Hum. Cell* **35**, 441–447 (2022).
17. van Bruggen, J. A. C. et al. Chronic lymphocytic leukemia cells impair mitochondrial fitness in $CD8^+$ T cells and impede CAR T-cell efficacy. *Blood* **134**, 44–58 (2019).
18. Good, C. R. et al. An NK-like CAR T cell transition in CAR T cell dysfunction. *Cell* **184**, 6081–6100 (2021).
19. Miranda, L. et al. AMP-activated protein kinase induces actin cytoskeleton reorganization in epithelial cells. *Biochem. Biophys. Res. Commun.* **396**, 656–661 (2010).
20. Garcia, D. & Shaw, R. J. AMPK: mechanisms of cellular energy sensing and restoration of metabolic balance. *Mol. Cell* **66**, 789–800 (2017).
21. Malik, N. et al. Induction of lysosomal and mitochondrial biogenesis by AMPK phosphorylation of FNIP1. *Science* **380**, eabj5559 (2023).
22. Bandey, I. N. et al. Designed improvement to T-cell immunotherapy by multidimensional single cell profiling. *J. Immunother. Cancer* **9**, e001877 (2021).
23. Chen, G. M. et al. Integrative bulk and single-cell profiling of premanufacture T-cell populations reveals factors mediating long-term persistence of CAR T-cell therapy. *Cancer Discov.* **11**, 2186–2199 (2021).
24. Haradhvala, N. J. et al. Distinct cellular dynamics associated with response to CAR-T therapy for refractory B cell lymphoma. *Nat. Med.* **28**, 1848–1859 (2022).
25. Wilson, T. L. et al. Common trajectories of highly effective CD19-specific CAR T cells identified by endogenous T cell receptor lineages. *Cancer Discov.* **12**, 2098–2119 (2022).
26. Dupre, L., Houmadi, R., Tang, C. & Rey-Barroso, J. T lymphocyte migration: an action movie starring the actin and associated actors. *Front. Immunol.* **6**, 586 (2015).
27. You, R. et al. Active surveillance characterizes human intratumoral T cell exhaustion. *J. Clin. Invest.* **131**, e144353 (2021).
28. Dominguez Conde, C. et al. Cross-tissue immune cell analysis reveals tissue-specific features in humans. *Science* **376**, eabl5197 (2022).
29. Zhang, L. et al. Lineage tracking reveals dynamic relationships of T cells in colorectal cancer. *Nature* **564**, 268–272 (2018).
30. Jiao, S. et al. Intratumor expanded T cell clones can be non-sentinel lymph node derived in breast cancer revealed by single-cell immune profiling. *J. Immunother. Cancer* **10**, e003325 (2022).
31. Bhatt, D. et al. STARTRAC analyses of scRNAseq data from tumor models reveal T cell dynamics and therapeutic targets. *J. Exp. Med.* **218**, e20201329 (2021).
32. Zhang, J. A.-O. et al. Non-viral, specifically targeted CAR-T cells achieve high safety and efficacy in B-NHL. *Nature* **609**, 369–374 (2022).
33. Liadi, I. et al. Individual motile $CD4^+$ T cells can participate in efficient multikilling through conjugation to multiple tumor cells. *Cancer Immunol. Res.* **3**, 473–482 (2015).
34. Melenhorst, J. J. et al. Decade-long leukaemia remissions with persistence of $CD4^+$ CAR T cells. *Nature* **602**, 503–509 (2022).
35. Jacobelli, J. et al. Confinement-optimized three-dimensional T cell amoeboid motility is modulated via myosin IIA-regulated adhesions. *Nat. Immunol.* **11**, 953–961 (2010).
36. Fousek, K. et al. CAR T-cells that target acute B-lineage leukemia irrespective of CD19 expression. *Leukemia* **35**, 75–89 (2021).
37. Bielamowicz, K. et al. Trivalent CAR T cells overcome interpatient antigenic variability in glioblastoma. *Neuro. Oncol.* **20**, 506–518 (2018).
38. Fraietta, J. A. et al. Determinants of response and resistance to CD19 chimeric antigen receptor (CAR) T cell therapy of chronic lymphocytic leukemia. *Nat. Med.* **24**, 563–571 (2018).
39. Fellows, E., Gil-Parrado, S., Jenne, D. E. & Kurschus, F. C. Natural killer cell-derived human granzyme H induces an alternative, caspase-independent cell-death program. *Blood* **110**, 544–552 (2007).
40. Bourque, J., Kousnetsov, R. & Hawiger, D. Roles of HOPX in the differentiation and functions of immune cells. *Eur. J. Cell Biol.* **101**, 151242 (2022).
41. Scharping, N. E. et al. The tumor microenvironment represses T cell mitochondrial biogenesis to drive intratumoral T cell metabolic insufficiency and dysfunction. *Immunity* **45**, 374–388 (2016).
42. Mrass, P. et al. Random migration precedes stable target cell interactions of tumor-infiltrating T cells. *J. Exp. Med.* **203**, 2749–2761 (2006).
43. Breart, B., Lemaitre, F., Celli, S. & Bousso, P. Two-photon imaging of intratumoral $CD8^+$ T cell cytotoxic activity during adoptive T cell therapy in mice. *J. Clin. Invest.* **118**, 1390–1397 (2008).
44. Boulch, M. et al. A cross-talk between CAR T cell subsets and the tumor microenvironment is essential for sustained cytotoxic activity. *Sci. Immunol.* **6**, eabd4344 (2021).
45. Zinselmeyer, B. H. et al. PD-1 promotes immune exhaustion by inducing antiviral T cell motility paralysis. *J. Exp. Med.* **210**, 757–774 (2013).
46. Bhat, P., Leggatt, G., Waterhouse, N. & Frazer, I. H. Interferon-λ derived from cytotoxic lymphocytes directly enhances their motility and cytotoxicity. *Cell Death Dis.* **8**, e2836 (2017).
47. Krummel, M. F., Bartumeus, F. & Gerard, A. T cell migration, search strategies and mechanisms. *Nat. Rev. Immunol.* **16**, 193–201 (2016).
48. Hammer, J. A., Wang, J. C., Saeed, M. & Pedrosa, A. T. Origin, organization, dynamics, and function of actin and actomyosin networks at the T cell immunological synapse. *Annu. Rev. Immunol.* **37**, 201–224 (2019).
49. Kawalekar, O. U. et al. Distinct signaling of coreceptors regulates specific metabolism pathways and impacts memory development in CAR T cells. *Immunity* **44**, 380–390 (2016).

50. van der Windt, G. J. et al. Mitochondrial respiratory capacity is a critical regulator of CD8$^+$ T cell memory development. *Immunity* **36**, 68–78 (2012).
51. Schaffer, B. E. et al. Identification of AMPK phosphorylation sites reveals a network of proteins involved in cell invasion and facilitates large-scale substrate prediction. *Cell Metab.* **22**, 907–921 (2015).
52. Georgiadou, M. et al. AMPK negatively regulates tensin-dependent integrin activity. *J. Cell Biol.* **216**, 1107–1121 (2017).
53. Mulazzani, M. et al. Long-term in vivo microscopy of CAR T cell dynamics during eradication of CNS lymphoma in mice. *Proc. Natl Acad. Sci. USA* **116**, 24275–24284 (2019).
54. Slaats, J. et al. Metabolic screening of cytotoxic T-cell effector function reveals the role of CRAC channels in regulating lethal hit delivery. *Cancer Immunol. Res.* **9**, 926–938 (2021).
55. Liadi, I., Roszik, J., Romain, G., Cooper, L. J. & Varadarajan, N. Quantitative high-throughput single-cell cytotoxicity assay for T cells. *J. Vis. Exp.* **2**, e50058 (2013).
56. An, X. et al. Single-cell profiling of dynamic cytokine secretion and the phenotype of immune cells. *PLoS ONE* **12**, e0181904 (2017).
57. Romain, G. et al. Antibody Fc engineering improves frequency and promotes kinetic boosting of serial killing mediated by NK cells. *Blood* **124**, 3241–3249 (2014).
58. Tinevez, J. Y. et al. TrackMate: an open and extensible platform for single-particle tracking. *Methods* **115**, 80–90 (2017).
59. Hao, Y. et al. Integrated analysis of multimodal single-cell data. *Cell* **184**, 3573–3587 (2021).
60. Huang, M. et al. SAVER: gene expression recovery for single-cell RNA sequencing. *Nat. Methods* **15**, 539–542 (2018).
61. Hanzelmann, S., Castelo, R. & Guinney, J. GSVA: gene set variation analysis for microarray and RNA-seq data. *BMC Bioinformatics* **14**, 7 (2013).
62. Jena, B. et al. Chimeric antigen receptor (CAR)-specific monoclonal antibody to detect CD19-specific T cells in clinical trials. *PLoS ONE* **8**, e57838 (2013).
63. Singh, H. et al. Reprogramming CD19-specific T cells with IL-21 signaling can improve adoptive immunotherapy of B-lineage malignancies. *Cancer Res.* **71**, 3516–3527 (2011).

Acknowledgements

This publication was supported by the NIH (R01GM143243, to N.V.), CPRIT (RP180466, to N.V.), MRA Established Investigator Award (509800, to N.V.), NSF (1705464, to N.V.), CDMRP (CA160591, to N.V.) and Owens foundation (to N.V.). scRNA-seq was performed at the Single Cell Genomics Core at Baylor College of Medicine supported by the NIH shared instrument grants S10OD018033, S10OD023469, S10OD025240 and P30EY002520 to Rui Chen. Sequencing was performed at the Genomic and RNA Profiling Core at Baylor College of Medicine with funding from the NIH NCI (P30CA125123) and CPRIT (RP200504). We would like to acknowledge the MD Anderson Cancer Center Flow Cytometry and Cellular Imaging Core facility for FACS sorting (NCI P30CA16672), Intel for the loan of the computing cluster and the Research Computing Data Core at the University of Houston for the use of the Carya and Sabine clusters.

Author contributions

A.R., G.R., S.N., L.J.N.C., H.S. and N.V. designed the study. A.R., G.R., M.F., H.S., S.N., M.J.M., N.V. and L.J.N.C. prepared the paper. A.R., G.R., M.F., M.M.P., K.F., X.A., F.S., M.J.M. and I.N.B. performed the experiments. A.R., G.R., M.F., A.S., M.M.P., X.A., N.A., J.R.T.A., M.J.M. and F.S. analyzed the data. H.S., L.J.N.C., S.N., N.P.O., A.B., C.B., M.M. and D.H. provided human samples. All authors edited and approved the paper.

Competing interests

L.J.N.C. and N.V. are cofounders of CellChorus that licensed TIMING from University of Houston. N.V. is a cofounder of AuraVax Therapeutics. L.J.N.C. has equity ownership in Alaunos Oncology (formerly Ziopharm Oncology). The Sleeping Beauty system for CD19-specific CAR T cells is licensed including to Ziopharm Oncology. M.F. is an employee of CellChorus. None of these conflicts of interest influenced any part of the study design or results. The remaining authors declare no competing interests.

Additional information

Extended data is available for this paper at https://doi.org/10.1038/s43018-024-00768-3.

Supplementary information The online version contains supplementary material available at https://doi.org/10.1038/s43018-024-00768-3.

Correspondence and requests for materials should be addressed to Navin Varadarajan.

Peer review information *Nature Cancer* thanks Michael Dustin, Frederick Locke and the other, anonymous, reviewer(s) for their contribution to the peer review of this work.

https://doi.org/10.1038/s43018-024-00768-3

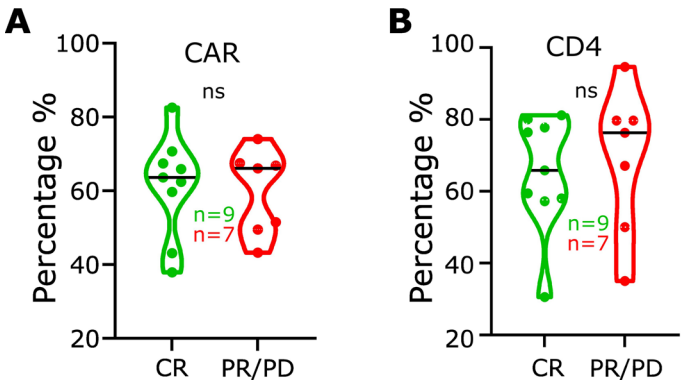

Extended Data Fig. 1 | Phenotype characteristics of infusion products measured by flow cytometry. (**a**) Comparisons of CAR + T cells recorded by flow cytometry for all sixteen patients (n). There is no significant difference in the CAR frequency between CR and PR/PD. (**b**) Comparisons of CD4 + T cells recorded by flow cytometry for all sixteen patients (n). There is no significant difference in the CD4 frequency between CR and PR/PD.

https://doi.org/10.1038/s43018-024-00768-3

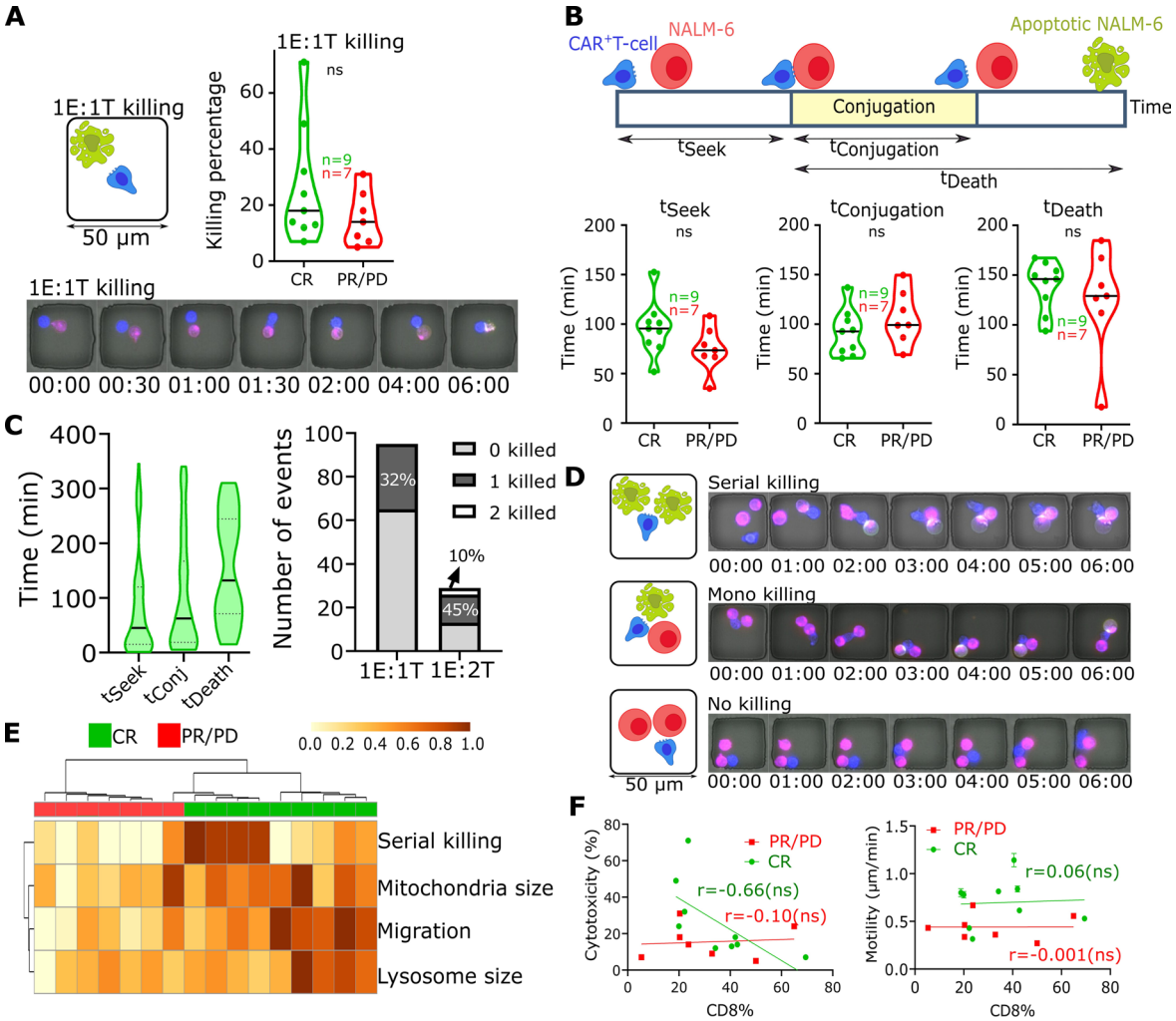

Extended Data Fig. 2 | T cells from CR are enriched for serial killing, increasing mitochondrial and lysosomal size, and persistent migration. (**a**) Schematic of a killing event at an E:T of 1:1 in which a CAR T-cell conjugates and kills a NALM-6 cell. The plot on the right shows the killing rate comparison between T cells from CR and PR/PD within all 1E:1T nanowells. Each dot (n) represents the frequency of killer T cells for each IP. Micrograph showing an example of 1E:1T killing event through the 6-hours (hh:mm) of time-lapse imaging from a CR IP. (**b**) Schematic of a killing event, showing the interaction parameters. tSeek defined as the time for CAR-T cell to find and conjugate to the NALM-6 cell. tconjugation is defined as the duration of CAR-T cell in stable conjugation with NALM-6 cell. tDeath is the time interval between the start of the conjugation and the apoptosis of the NALM-6 cell. Plots show the comparison between T cells from CR and PD/PR for these parameters. Each dot (n) represents the average value for all T cells within each IP. (**c**) Representative violin plot shows the interaction parameters from one responder IP: tSeek (n = 96 events), tconjugation (n = 94 events), tDeath (n = 30 events). The bar graph shows the killing frequencies of the same responder IP at an E:T of both 1:1 and 1:2. (**d**) Schematics and examples of serial killing, mono killing and no-killing events in nanowells with an E:T of 1:2. (**e**) Unsupervised hierarchical clustering based on parameters from TIMING, and confocal microscopy. Serial killing, migration, increasing mitochondrial and lysosomal volume were features associated with T cells from CR patients. (**f**) Cytotoxicity and motility correlations with CD4/CD8 ratio. Each point represents the average parameter for each IP (n = 9 patient IPs). Cytotoxicity is defined as the frequency of 1E:1T killing from TIMING. The Pearson's correlation coefficient was calculated for CR and PR/PD IP.

https://doi.org/10.1038/s43018-024-00768-3

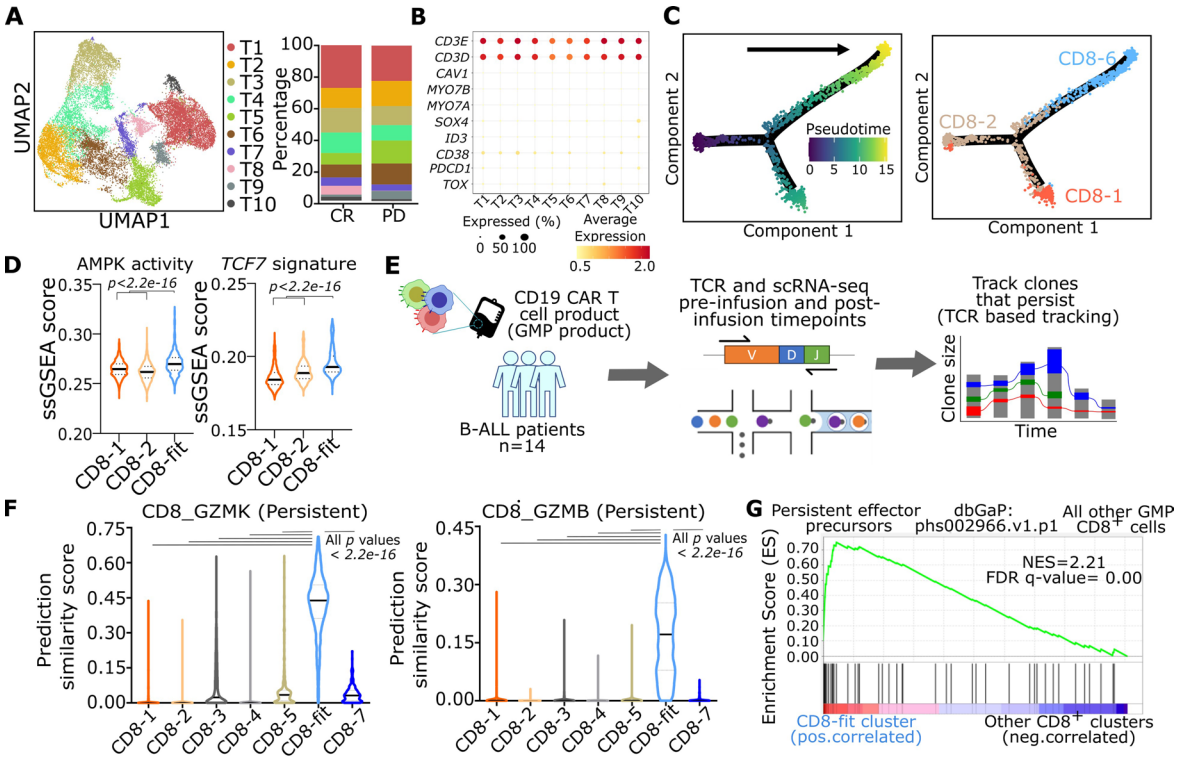

Extended Data Fig. 3 | T-cell phenotypes defined using scRNA-seq. (**a**) Uniform Manifold Approximation and Projection (UMAP) for 21,469 cells from nine IPs. Bar graph showing the distribution of T cells from CR and PD/PR among 10 clusters determined using unsupervised clustering. (**b**) Bubble plot showing key genes associated with T-cell migration and exhaustion phenotypes. (**c**) Pseudotime trajectory analysis for two clusters enriched in PD (CD8-1: n = 572 cells, CD8-2: n = 1,031 cells) and one cluster enriched in CR (CD8-6: n = 1,253 cells). Necklace plots show CD8-2 (Central Memory dominant) differentiate into Effector/Effector Memory dominant CD8-fit (CD8-6) and CD8-1. (**d**) Violin plot (left) showing the ssGSEA score for AMPK activation calculated for two clusters enriched in PD (CD8-1: n = 572 cells, CD8-2: n = 1,031 cells) and CD8-fit (CD8-6: n = 1,253 cells) cluster enriched in CR. Violin plot (right) showing the ssGSEA score for the *TCF7* signature for the three clusters. The black bar represents the median and the dotted lines denote quartiles. *P* values were computed using two-tailed Welch's T-test. (**e**) Schematic overview of the experimental process used to identify signatures of persistent CAR T cells. Single-cell gene expression and T-cell receptor (TCR) datasets were generated by sequencing pre- (GMP: good manufacturing practice facility) and post-infusion CD19 CAR T cells from blood and bone marrow samples of pediatric patients with B-ALL. (**f**) Violin plots showing the transcriptome similarities between the $CD8^+$ T cells from our datasets and $CD8^+$ GMP effector precursors. P values were calculated using two-tailed t-test. The black bar represents the median and the dotted lines denote quartiles. *P* values were computed using two-tailed Welch's T-test. (**g**) Gene set enrichment analysis (GSEA) of $CD8^+$ GMP effector precursors gene signatures within cells from CD8-fit cluster compared with cells from all other CD8 clusters. The effector precursors gene signature is based on differentially expressed genes between the $CD8^+$ effector precursors clusters and all other GMP $CD8^+$ T cells from part E.

https://doi.org/10.1038/s43018-024-00768-3

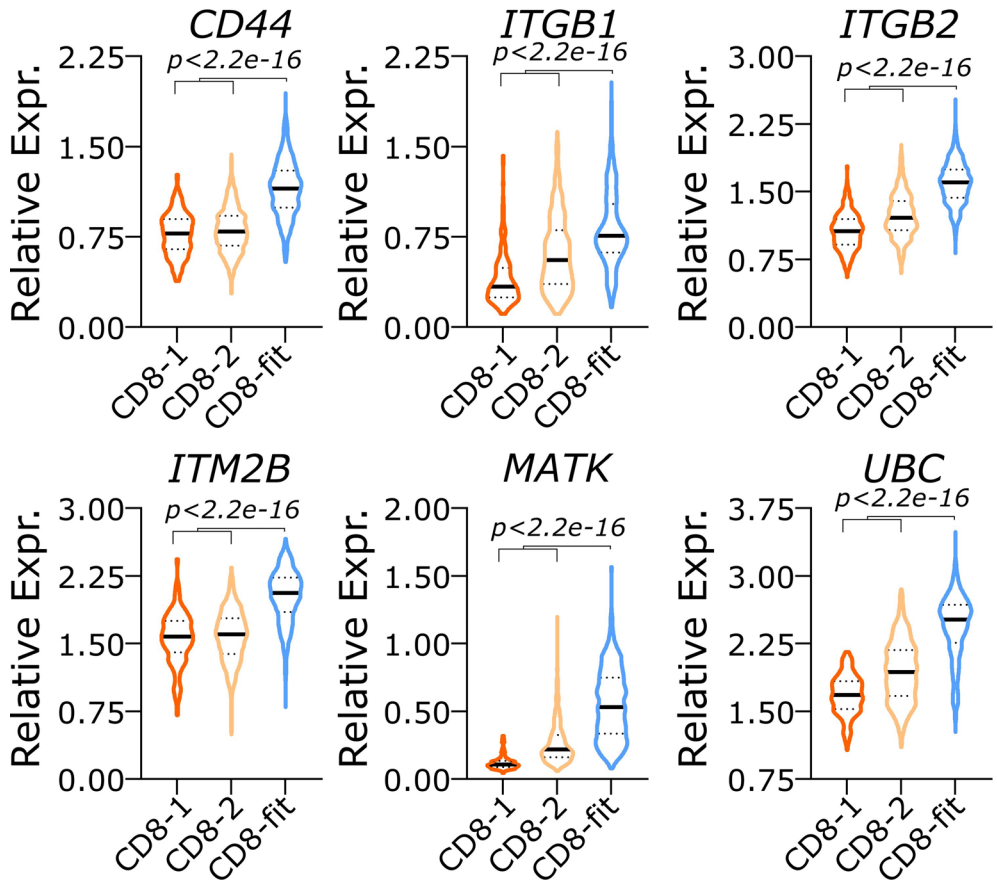

Extended Data Fig. 4 | Matrix binding genes are significantly upregulated in the CD8-fit population. Violin plots showing the expression of matrix binding genes enriched in CD8-fit cluster (CD8-1: n = 572 cells, CD8-2: n = 1,031 cells, CD8-fit: n = 1,253 cells). The black bar represents the median and the dotted lines denote quartiles. *P* values were computed using two-tailed Welch's T-test.

https://doi.org/10.1038/s43018-024-00768-3

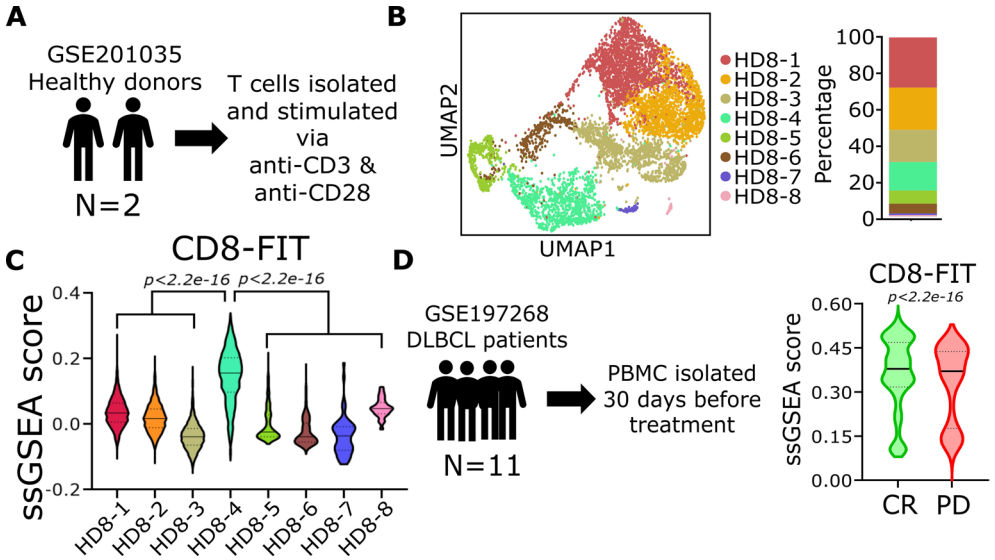

Extended Data Fig. 5 | CD8-fit cells can be identified in healthy donor derived T cells and in the premanufacture PBMCs of patients treated with CAR T cells. (**a**) Overview of external dataset study GSE201035. (**b**) Uniform Manifold Approximation and Projection (UMAP) for 6,713 cells from two donors. Bar graph showing the distribution of $CD8^+$ T cells among 8 clusters determined using unsupervised clustering. (**c**) Violin plot showing the CD8-fit ssGSEA score comparison between the 8 healthy donor CD8 + T-cell clusters. For the violin plot, the black bar represents the median and the dotted lines denote quartiles. *P* values were computed using one-way ANOVA with Holm-Šídák's multiple comparisons test. (**d**) Validation of the association between CD8-fit and clinical responses in pre-manufactured T cells. Single-cell gene expression datasets were generated by sequencing pre-manufactured T cells from patients with B-cell lymphoma. ssGSEA-derived migration scores between $CD8^+$ T cells from CR (n = 13,930) and PD (n = 3,679) were computed. For the violin plot, the black bar represents the median and the dotted lines denote quartiles. *P* value was computed using two-tailed Welch's T-test.

https://doi.org/10.1038/s43018-024-00768-3

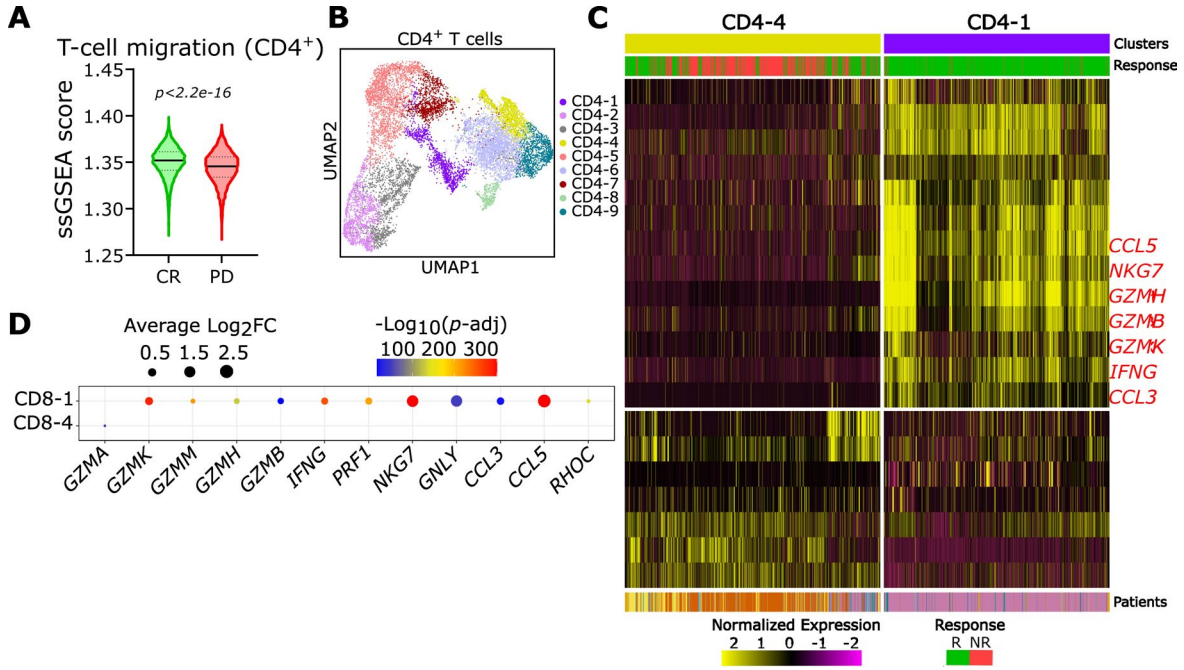

Extended Data Fig. 6 | CD4⁺T-cell phenotypes defined using scRNA-seq. (**a**) Comparisons of the T-cell migration scores between all CD4⁺ T cells (n = 12,527) from 9 CR and PD/PR IPs. The black bar represents the median and the dotted lines denote quartiles. *P* values were computed using two-tailed Welch's T-test. (**b**) UMAP for CD4⁺ T cells (n = 12,527). Nine clusters were identified using unsupervised clustering. (**c**) Heat map of two CD4⁺ T-cell clusters generated by unsupervised clustering. CD4-4 mostly cells from PR/PD while CD4-1 are enriched with CR cells. A color-coded track on top shows the cells from infusion products of CR (green) and PR/PD (red). The track below the heatmap, shows the sample origin for each cell. (**d**) Bubble plot showing key genes differentially expressed among CD4⁺ T clusters. P value was calculated using the Wilcoxon rank sum test with Bonferroni correction.

https://doi.org/10.1038/s43018-024-00768-3

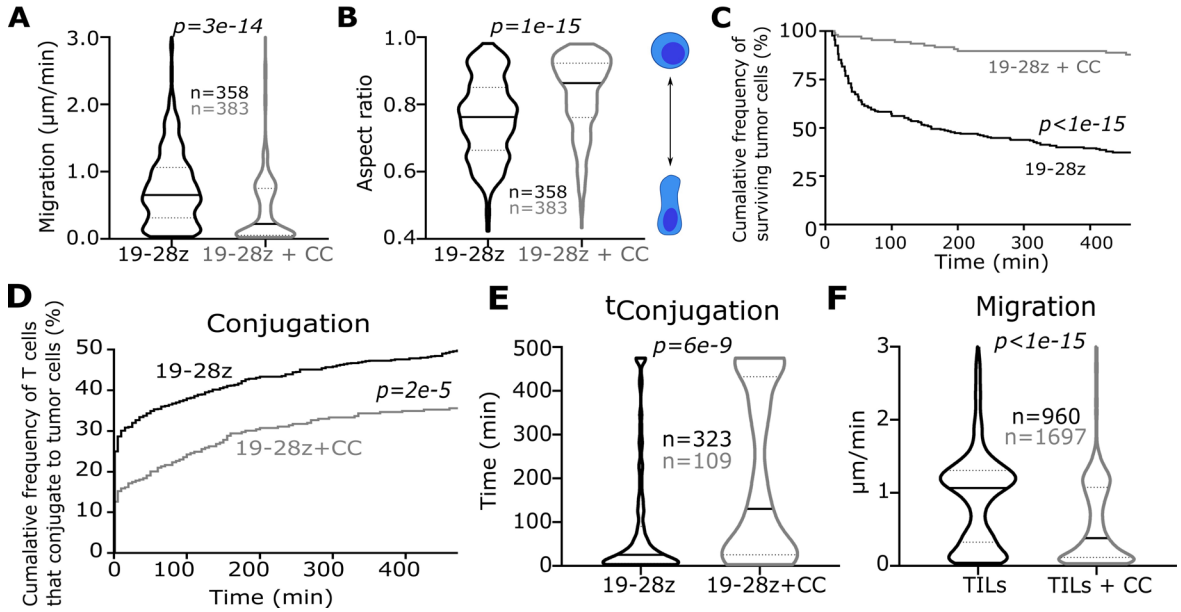

Extended Data Fig. 7 | The impact of AMPK inhibition on T cell antitumor function revealed by TIMING. (A/B) (**a, b**) The migration and polarization of 19-28z T cells treated with Compound C (CC). All data representative of three independent experiments with 19-28z T cells from three healthy human donors at an E:T of 1:1. The black bar represents the median and the dotted lines denote quartiles. The *P* value was computed using a two-tailed Welch's t-test. (**c**) Comparisons of the killing frequency of vehicle treated (DMSO) or CC treated 19-28z CAR T cells. Each data point represents a single cell. *P* value was computed using two-tailed log-rank test. (**d**) The cumulative frequency of T cells conjugating to tumors cells over 8 hours. *P* value was computed using two-tailed log-rank test. (**e**) The duration of conjugation between individual T cells and tumor cells. Each data point represents a single cell. The black bar represents the median and the dotted lines denote quartiles. The *P* value was computed using a two-tailed Welch's t-test. (**f**) The impact of AMPK inhibition on migrating capabilities of expanded tumor infiltrating lymphocytes (TILs) from melanoma patients. The migration speed of individual TILs as measured by TIMING (1E:0T). Each data point represents average migration for a single cell. The black bar represents the median and the dotted lines denote quartiles. *P* value was computed using two-tailed Welch's t-test.

https://doi.org/10.1038/s43018-024-00768-3

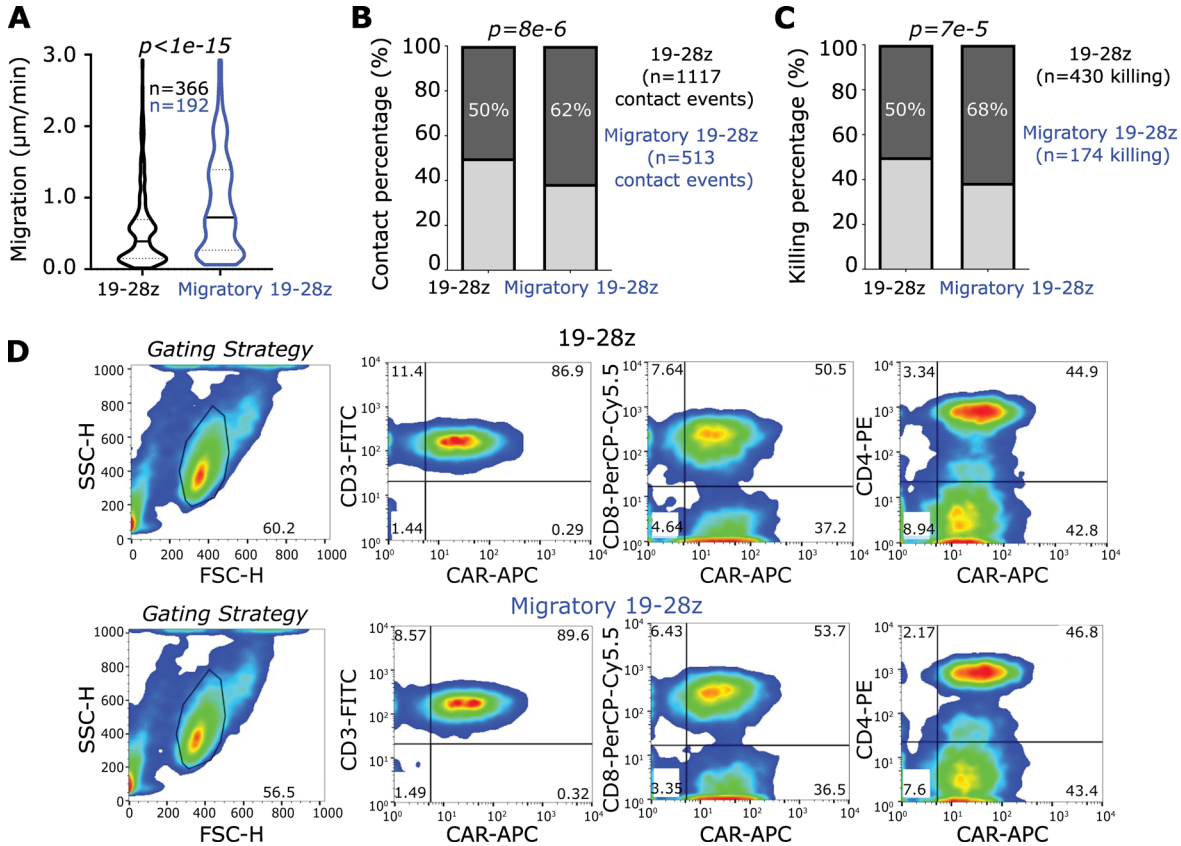

Extended Data Fig. 8 | Enrichment and functional characterization of migratory 19-28z T cells. (**a**) Comparisons between the migration of migrated (migratory) and unsorted cells as measured by TIMING (1E:0T). The black bar represents the median and the dotted lines denote quartiles. *P* value was computed using two-tailed Welch's t-test. (**b**) The frequency of conjugation of T cells to tumor cells comparing migratory and unsorted 19-28z T cells evaluated using TIMING (1E:1T). *P* value was computed using a two-tailed chi-square test. (**c**) Killing percentage of migratory and unsorted 19-28z T cells evaluated using TIMING (1E:1T). *P* value was computed using a two-tailed chi-square test. (**d**) Phenotyping of matched 19-28z and migratory 19-28z T-cell populations. This data is representative of at least four healthy donor-derived T-cell populations measured by flow cytometry. Gating strategies are shown from the side scatter and forward scatter panels on the far left.

https://doi.org/10.1038/s43018-024-00768-3

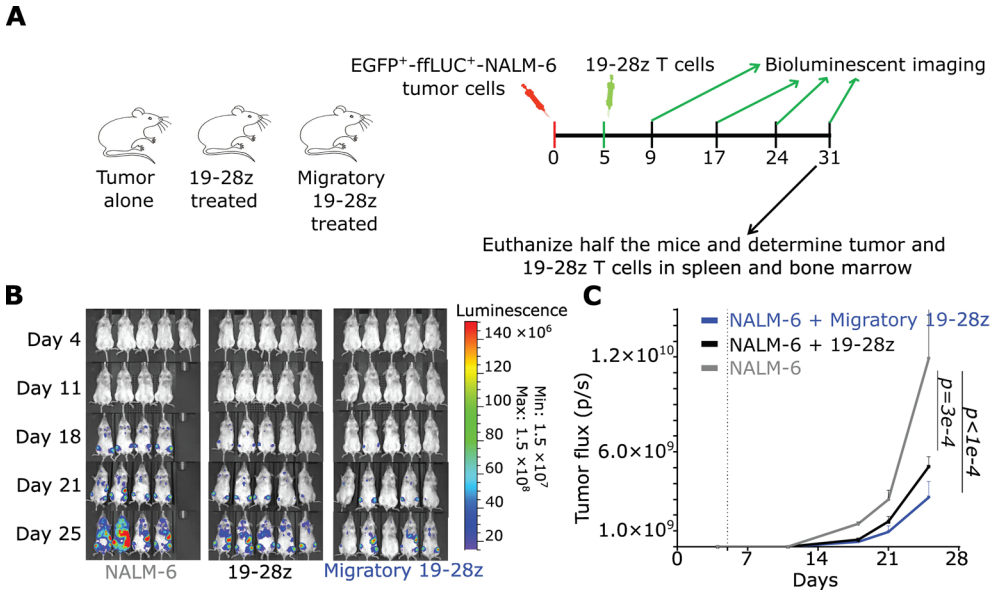

Extended Data Fig. 9 | Migratory 19-28z T cells showed enhanced antitumor activity compared to the unsorted 19-28z T cells in suboptimal dose model. (**a**) Design of mice experiments to determine the relative efficacy of the 19-28z populations. Mice were treated with either 19-28z T cells or migratory 19-28z T cells five days after the injection of ffLuc expressing EGFP + NALM-6 cells. The mice were euthanized on day 31 and five mice from each of the two T-cell treated groups was used to quantify both the tumor cells and persisting T cells within the spleen and bone marrow of mice. (**b**) False-colored images illustrating the photon flux from ffLuc expressing EGFP$^+$NALM-6 cells treated with suboptimal doses of 19-28z T cells. (**c**) Time course of the longitudinal measurements of NALM-6 derived photon flux from the three separate cohorts of mice (n = 5 in each group). The dotted line marks the day (Day 5) where 19-28z T cells were introduced into the mice. The background luminescence was defined based on mice with no tumor. Error bars represent SEM and *P* values were computed using a two-tailed Mann-Whitney t-test.

https://doi.org/10.1038/s43018-024-00768-3

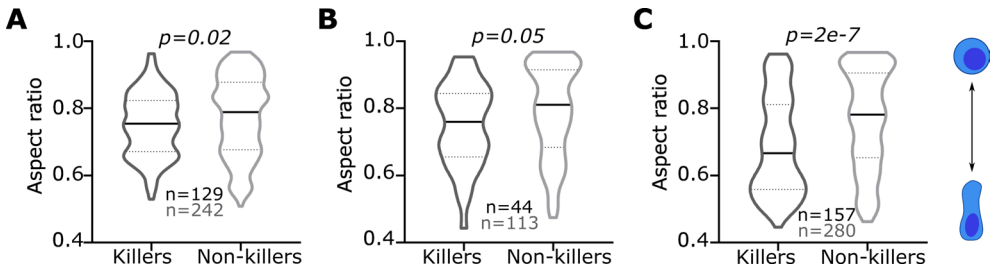

Extended Data Fig. 10 | Quantifying the link between migration and functionality in diverse CARs. (**a**–**c**) The polarization (reflective of the morphology of migratory cells) of individual killer and nonkiller CAR T cells without and with conjugation to tumor cells. All data from an E:T of 1:1. (A) shows the data for 19-8-28z T cells tested against NALM-6 cells. (B) and (C) show the data for two different constructs of tri-specific CAR$^+$ T cells tested against patient-derived tumor cells. The black bar represents the median and the dotted lines denote quartiles. All *P* values were computed using two-tailed t-tests and each data point represents a single effector cell.

nature portfolio

Corresponding author(s): Varadarajan, Navin

Last updated by author(s): Mar 26, 2024

Reporting Summary

Nature Portfolio wishes to improve the reproducibility of the work that we publish. This form provides structure for consistency and transparency in reporting. For further information on Nature Portfolio policies, see our Editorial Policies and the Editorial Policy Checklist.

Statistics

For all statistical analyses, confirm that the following items are present in the figure legend, table legend, main text, or Methods section.

n/a	Confirmed
☐	☒ The exact sample size (*n*) for each experimental group/condition, given as a discrete number and unit of measurement
☐	☒ A statement on whether measurements were taken from distinct samples or whether the same sample was measured repeatedly
☐	☒ The statistical test(s) used AND whether they are one- or two-sided *Only common tests should be described solely by name; describe more complex techniques in the Methods section.*
☐	☒ A description of all covariates tested
☐	☒ A description of any assumptions or corrections, such as tests of normality and adjustment for multiple comparisons
☐	☒ A full description of the statistical parameters including central tendency (e.g. means) or other basic estimates (e.g. regression coefficient) AND variation (e.g. standard deviation) or associated estimates of uncertainty (e.g. confidence intervals)
☐	☒ For null hypothesis testing, the test statistic (e.g. *F*, *t*, *r*) with confidence intervals, effect sizes, degrees of freedom and *P* value noted *Give P values as exact values whenever suitable.*
☒	☐ For Bayesian analysis, information on the choice of priors and Markov chain Monte Carlo settings
☒	☐ For hierarchical and complex designs, identification of the appropriate level for tests and full reporting of outcomes
☐	☒ Estimates of effect sizes (e.g. Cohen's *d*, Pearson's *r*), indicating how they were calculated

Our web collection on statistics for biologists contains articles on many of the points above.

Software and code

Policy information about availability of computer code

Data collection	Confocal images were collected using NIS-Elements AR v 5.11.01. Microscopy images from TIMING were collected using ZEN PRO v2.6. Flow cytometry readings were collected using FlowJo v10.8. Mice images using IVIS were collected using Living Image v2.50.1.
Data analysis	Confocal images were analyzed using the following ImageJ plugins: Subtract background, 3D objects counter, TrackMate. ScRNAseq FASTQ files obtained from sequencing core were processed using CellRanger v6.0. ScRNAseq data was analyzed in R v4.0.1 with the following packages: Seurat v4.1, SAVER v1.1.2, GSVA v0.3.4, Monocle v2.26. TIMING tracking and images were analyzed using a custom pipeline developed by the Varadarajan lab.

For manuscripts utilizing custom algorithms or software that are central to the research but not yet described in published literature, software must be made available to editors and reviewers. We strongly encourage code deposition in a community repository (e.g. GitHub). See the Nature Portfolio guidelines for submitting code & software for further information.

Data

Policy information about availability of data

All manuscripts must include a data availability statement. This statement should provide the following information, where applicable:

- Accession codes, unique identifiers, or web links for publicly available datasets
- A description of any restrictions on data availability
- For clinical datasets or third party data, please ensure that the statement adheres to our policy

The scRNA-seq of the infusion products is available under GEO accession number GSE208052 and migratory CAR T-cell scRNA-seq is available under GEO accession number GSE253872. External datasets used for CD8-fit signature validation were accessed under GEO accession numbers GSE197268 and GSE151511 and EMBL-EBI accession number E-MTAB-11536. The external dataset used for T-cell persistence was accessed via dbGaP under Study Accession phs002966.v1.p1. The healthy donor T-cell scRNA-seq was accessed under GSE201035. Source data for Fig. 2, 4, 5, 6 and Extended Data Fig. 1-2, 7-10 have been provided as Source Data files. All other data supporting the findings of this study are available from the corresponding author on reasonable request.

Research involving human participants, their data, or biological material

Policy information about studies with human participants or human data. See also policy information about sex, gender (identity/presentation), and sexual orientation and race, ethnicity and racism.

Reporting on sex and gender	No sex or gender analysis was performed.
Reporting on race, ethnicity, or other socially relevant groupings	No reporting on race, ethnicity, or other socially relevant groupings was conducted for this study.
Population characteristics	For the infusion products, patients had pre-existing DLBCL prior to standard of care treatment. For human blood donations, whole blood was coded and negative for viral markers. For TILs, information regarding population characteristics can be found at https://clinicaltrials.gov/study/NCT00338377.
Recruitment	For the infusion products, patients with DLBCL were selected. For human blood donations, healthy donors need to meet the criteria established by the Gulf Coast Regional Blood Center. For TILs, information regarding recruitment of patients can be found in detail at https://clinicaltrials.gov/study/NCT00338377.
Ethics oversight	All work pertaining to the infusion products outlined in this report was performed according to protocols approved by the Institutional Review Boards at the University of Houston and the University of Texas MD Anderson Cancer Center. Patients provided written informed consent. Blood donations via the Gulf Coast Regional Blood Center are subject to FDA regulation and state agencies. Donors provide written informed consent. For TILs, protocol (2004–0069) was approved by the Institutional Review Board (IRB) of the University of Texas MD Anderson Cancer Center (Houston, TX) and an FDA-approved Investigational New Drug (IND) application (NCT00338377). More information can be found at can be found in detail at https://clinicaltrials.gov/study/NCT00338377. Patients provided written informed consent for use of their samples.

Note that full information on the approval of the study protocol must also be provided in the manuscript.

Field-specific reporting

Please select the one below that is the best fit for your research. If you are not sure, read the appropriate sections before making your selection.

☒ Life sciences ☐ Behavioural & social sciences ☐ Ecological, evolutionary & environmental sciences

For a reference copy of the document with all sections, see nature.com/documents/nr-reporting-summary-flat.pdf

Life sciences study design

All studies must disclose on these points even when the disclosure is negative.

Sample size	No statistical methods were used to predetermine sample sizes for the infusion products or animal studies.
Data exclusions	No data was excluded from the analysis except for TIMING results. Time of conjugation and time of death events lower than 10 minutes were omitted from analysis; time of conjugation lower than 10 minutes assumes no synapse formation and time of death lower than 10 minutes can be attributed to spontaneous cell death.
Replication	Experiments using infusion products were not subject to technical replications due to limited number of cells. Mice models used biological replicates. TIMING experiments using in-house CAR T cells were repeated three times with all data presented.
Randomization	Animal studies used were subject to randomization.
Blinding	The researchers were not blinded to allocation during experiments and outcome assessment. Data collection and analysis were not performed blind to the conditions of the experiments.

Reporting for specific materials, systems and methods

We require information from authors about some types of materials, experimental systems and methods used in many studies. Here, indicate whether each material, system or method listed is relevant to your study. If you are not sure if a list item applies to your research, read the appropriate section before selecting a response.

Materials & experimental systems

n/a	Involved in the study
☐	☒ Antibodies
☐	☒ Eukaryotic cell lines
☒	☐ Palaeontology and archaeology
☐	☒ Animals and other organisms
☐	☒ Clinical data
☒	☐ Dual use research of concern
☒	☐ Plants

Methods

n/a	Involved in the study
☒	☐ ChIP-seq
☐	☒ Flow cytometry
☒	☐ MRI-based neuroimaging

Antibodies

Antibodies used: Anti-CD62L (Clone:DREG-56, Cat. 304827) [Dilution 1:20], Anti-CD45RA (Clone:HI100, Cat. 304111)[Dilution 1:20], Anti-CD3 (Clone: SK7, Cat. 981004)[Dilution 1:20], Anti-CD4 (Clone:OKT4, Cat. 317415)[Dilution 1:20], Anti-CD8 (Clone:RPA-T8, Cat. 301008)[Dilution 1:20] and Anti-Granzyme B (Clone: QA16A02, Cat. 372203)[Dilution 1:20] from Biolegend. CAR was produced in-house.

Validation: Per the Biolegend website:
To ensure they are both specific and sensitive, we validate our antibodies through a variety of methods including:

1) Testing on multiple cell and tissue types with a variety of known expression levels.
2) Validation in multiple applications as a cross-check for specificity and to provide additional clarity for researchers.
3) Comparison to existing antibody clones.
4) Using cell treatments to modulate target expression, such as phosphatase treatment to ensure phospho-antibody specificity.

Eukaryotic cell lines

Policy information about cell lines and Sex and Gender in Research

Cell line source(s): NALM6-from ATCC, T cells isolated from whole blood

Authentication: None of the cells were authenticated

Mycoplasma contamination: All cell lines used tested negative for mycoplasma contamination

Commonly misidentified lines (See ICLAC register): No commonly misidentified cell line was used in the study.

Animals and other research organisms

Policy information about studies involving animals; ARRIVE guidelines recommended for reporting animal research, and Sex and Gender in Research

Laboratory animals: 7-week-old NOD.Cg-PrkdcscidIl2rgtm1wjl/SzJ (NSG) female mice. Mice were housed at room temperature (20-24C), had 12 hours light-dark cycles with low intensity, and humidity between 40-60%. Cages were at least 12in^2 in size. The limit for maximal tumor size is 2000 mm^3 according to IAUCU guidelines and the limit was not exceeded for this study.

Wild animals: This study did not involve wild animals.

Reporting on sex: Findings from the mouse tumor models are applicable only to female mice. NSG female mice can randomized and change groups, but males will kill each other if mixed from other groups.

Field-collected samples: Study did not involve collecting samples from the field.

Ethics oversight: All experiments were approved and in accordance with the Institutional Animal Care and Use Committee at the University of Houston.

Note that full information on the approval of the study protocol must also be provided in the manuscript.

Clinical data

Policy information about clinical studies

All manuscripts should comply with the ICMJE guidelines for publication of clinical research and a completed CONSORT checklist must be included with all submissions.

Clinical trial registration	NCT00338377
Study protocol	Full trial protocol can be found in https://clinicaltrials.gov/study/NCT00338377
Data collection	Clinical trial is ongoing and started in 2006. More data is available at https://clinicaltrials.gov/study/NCT00338377
Outcomes	Outcomes defined can be found in detail at https://clinicaltrials.gov/study/NCT00338377

Plants

Seed stocks	*Report on the source of all seed stocks or other plant material used. If applicable, state the seed stock centre and catalogue number. If plant specimens were collected from the field, describe the collection location, date and sampling procedures.*
Novel plant genotypes	*Describe the methods by which all novel plant genotypes were produced. This includes those generated by transgenic approaches, gene editing, chemical/radiation-based mutagenesis and hybridization. For transgenic lines, describe the transformation method, the number of independent lines analyzed and the generation upon which experiments were performed. For gene-edited lines, describe the editor used, the endogenous sequence targeted for editing, the targeting guide RNA sequence (if applicable) and how the editor was applied.*
Authentication	*Describe any authentication procedures for each seed stock used or novel genotype generated. Describe any experiments used to assess the effect of a mutation and, where applicable, how potential secondary effects (e.g. second site T-DNA insertions, mosiacism, off-target gene editing) were examined.*

Flow Cytometry

Plots

Confirm that:

☒ The axis labels state the marker and fluorochrome used (e.g. CD4-FITC).

☒ The axis scales are clearly visible. Include numbers along axes only for bottom left plot of group (a 'group' is an analysis of identical markers).

☒ All plots are contour plots with outliers or pseudocolor plots.

☒ A numerical value for number of cells or percentage (with statistics) is provided.

Methodology

Sample preparation	Isolated cells were washed with FACS buffer two times, blocked with human plasma for 30 minutes, then stained with respective antibodies for 1 hour.
Instrument	BD LSRFortessa X-20 cell analyzer
Software	FlowJo v10
Cell population abundance	In vitro populations expressed >40% of markers of interest; in vivo populations expressed <5% of markers of interest.
Gating strategy	Gating strategy was performed on the preliminary FSC/SSC plots. Boundary of the gating strategy is shown in Extended Data Fig. 8D.

☒ Tick this box to confirm that a figure exemplifying the gating strategy is provided in the Supplementary Information.